Faculty of Science, Medicine and Health - Papers: part A

Faculty of Science, Medicine and Health

1-1-2014

Geophysical constraints on deep weathering and water storage potential in the Southern Sierra Critical Zone Observatory

W. Steven Holbrook
University of Wyoming

Clifford S. Riebe
University of Wyoming

Mehrez Elwaseif
University of Wyoming

Jorden L. Hayes
University of Wyoming

Kyle Basler-Reeder
Colorado State University

See next page for additional authors

Recommended Citation

Geophysical constraints on deep weathering and water storage potential in the Southern Sierra Critical Zone Observatory

Abstract

The conversion of bedrock to regolith marks the inception of critical zone processes, but the factors that regulate it remain poorly understood. Although the thickness and degree of weathering of regolith are widely thought to be important regulators of the development of regolith and its water-storage potential, the functional relationships between regolith properties and the processes that generate it remain poorly documented. This is due in part to the fact that regolith is difficult to characterize by direct observations over the broad scales needed for process-based understanding of the critical zone. Here we use seismic refraction and resistivity imaging techniques to estimate variations in regolith thickness and porosity across a forested slope and swampy meadow in the Southern Sierra Critical Zone Observatory (SSCZO). Inferred seismic velocities and electrical resistivities image a weathering zone ranging in thickness from 10 to 35 m (average = 23 m) along one intensively studied transect. The inferred weathering zone consists of roughly equal thicknesses of saprolite (P-velocity < 2 km s−1) and moderately weathered bedrock (P-velocity = 2–4 km s−1). A minimum-porosity model assuming dry pore space shows porosities as high as 50% near the surface, decreasing to near zero at the base of weathered rock. Physical properties of saprolite samples from hand augering and push cores are consistent with our rock physics model when variations in pore saturation are taken into account. Our results indicate that saprolite is a crucial reservoir of water, potentially storing an average of 3 m3 m−2 of water along a forested slope in the headwaters of the SSCZO. When coupled with published erosion rates from cosmogenic nuclides, our geophysical estimates of weathering zone thickness imply regolith residence times on the order of 105 years. Thus, soils at the surface today may integrate weathering over glacial−interglacial fluctuations in climate.

Disciplines

Medicine and Health Sciences | Social and Behavioral Sciences

Publication Details

Authors

W. Steven Holbrook, Clifford S. Riebe, Mehrez Elwaseif, Jorden L. Hayes, Kyle Basler-Reeder, Dennis L. Harry, Armen Malazian, Anthony Dosseto, Peter C. Hartsough, and Jan W. Hapmans

Geophysical Constraints on Deep Weathering and Water Storage Potential in the Southern Sierra Critical Zone Observatory

W. Steven Holbrook[1], Clifford S. Riebe[1], Mehrez Elwaseif[1], Jorden Hayes[1], Kyle Reeder[2],

Dennis Harry[2], Armen Malazian[3], Anthony Dosseto[4], Peter Hartsough[3], and Jan Hopmans[3]

[1] Department of Geology and Geophysics, University of Wyoming, Laramie, WY 82071

[2] Department of Geosciences, Warner College of Natural Resources, Colorado State University, Ft Collins, CO 80523

[3] Department of Land, Air and Water Resources, University of California, Davis, CA 95616

[4] School of Earth and Environmental Science, University of Wollongong, Australia

Abstract

The conversion of bedrock to regolith marks the inception of critical zone processes, but the factors that regulate it remain poorly understood. Although the thickness and degree of weathering of regolith are widely thought to be important regulators of the development of regolith and its water-storage potential, the functional relationships between regolith properties and the processes that generate it remain poorly documented. This is due in part to the fact that regolith is difficult to characterize by direct observations over the broad scales needed for process-based understanding of the critical zone. Here we use seismic refraction and resistivity imaging techniques to estimate variations in regolith thickness and porosity across a forested slope and swampy meadow in the Southern Sierra Critical Zone Observatory (SSCZO). Inferred seismic velocities and electrical resistivities image a weathering zone ranging in thickness from 10 to 35 m (average = 23 m) along one intensively studied transect. The inferred weathering zone consists of roughly equal thicknesses of saprolite (P-velocity < 2 km/s) and moderately weathered bedrock (P-velocity 2-4 km/s). A minimum-porosity model assuming dry pore space shows porosities as high as 50% near the surface, decreasing to near zero at the base of weathered rock. Physical properties of saprolite samples from hand augering and push cores are consistent with our rock physics model when variations in pore saturation are taken into account. Our results indicate that saprolite is a crucial reservoir of water, potentially storing an average of 3 m^3/m^2 of water along a forested slope in the headwaters of the SSCZO. When coupled with published erosion rates from cosmogenic nuclides, our geophysical estimates of weathering zone thickness imply regolith residence times on the order of 10^5 years. Thus, soils at the SSCZO evidently integrate weathering over glacial-interglacial fluctuations in climate.

Introduction

In hilly and mountainous landscapes, bedrock breaks down in a complex interplay of physical, chemical, and biological processes. Damage from fracturing (e.g., Clarke and Burbank, 2011; Molnar et al., 2007), frost cracking (Anderson et al., 2013) and other mechanical processes enables subsurface penetration and throughflow of meteoric water. This in turn promotes chemical leaching, which causes solute losses (e.g., Stonestrom et al., 1998; Buss et al., 2008) and enhances the residuum's susceptibility to further weathering and erosion (Dixon et al., 2009). Add life, and the transformation from rock to soil is complete; tree roots pry remaining rock apart and, together with symbiotic fungi, exude organic compounds that liberate life-sustaining nutrients from minerals and generate water-holding pore space in the mycorrhizosphere (Banfield et al., 1999; Graham et al., 2010; Hubbert et al., 2001; Landeweert et al., 2001).

Regolith, which here refers collectively to saprolite and soil, is the foundation for life in the "critical zone" (CZ) (see Fig. 1 for definitions). Its creation by subsurface weathering is counteracted by losses due to chemical erosion at depth and by both chemical and physical erosion near the surface (Riebe and Granger, 2013; Dixon et al., 2009). The resulting competition between the creation and removal of regolith ultimately sets its thickness and degree of weathering (e.g., Anderson et al., 2007; Lebedeva et al., 2010; Stallard, 1985). For example, if erosion is fast and weathering is slow, such that the system is "weathering-limited" (Carson and Kirkby, 1972; Stallard and Edmond, 1983), regolith is typically thin and not extensively weathered. Alternatively, if erosion is slow and weathering is fast, such that the system is "transport-limited", regolith is typically thick and may be extensively weathered, due to long residence times afforded by slow removal rates. In this context, regolith is a residuum that can be interpreted in terms of the processes that created it (Stallard and Edmund, 1983). Yet regolith is not just a residuum, but also a matrix of critical zone processes. Hence regolith influences as

3

well as reflects the balance between weathering and erosion. For example, rates of soil production have often been observed to decrease with increasing soil thickness (Heimsath et al., 2012), consistent with the hypothesis that saprolite blanketed by thinner soils should be exposed to more frequent disruption by the biophysical processes that produce soil (Davis 1892; Gilbert 1909). This carries with it a negative feedback that may stabilize soils against wide fluctuations in thickness (Dietrich et al., 1995); changes in soil thickness are self-arresting due to their offsetting influence on soil production rates. Similar feedbacks between surface and subsurface processes may help regulate the thickness of the regolith as a whole (Lebedeva et al., 2010). For example, regolith production in the Rio Blanco Quartz Diorite (in Puerto Rico) appears to be driven by biotite oxidation in the presence of dissolved oxygen, which varies in porewaters as a function of depth in saprolite (Buss et al., 2008). This suggesting that regolith thickness may regulate regolith production rates in a hydro-geochemical feedback. Mechanisms such as this may help explain the growing body of empirical evidence from sites spanning a range of conditions that regolith properties may often play a role in setting the pace of regolith production (Dosseto et al., 2008; Ma et al., 2010; Dosseto et al., 2012). Understanding precisely how is fundamental to process-based understanding of critical zone formation and evolution. Making progress on this challenging problem requires knowledge of how the thickness and degree of alteration of regolith vary across landscapes (Brantley et al., 2011; Braun et al., 2009).

Probing regolith over scales appropriate to process-based studies of the critical zone is challenging. Regolith is often tens of meters thick and highly variable in space. Drilling can be expensive and provides point samples that may not be representative of the surrounding regolith. Digging pits and augering by hand is less expensive and easier to apply over broad scales (e.g., Burke et al., 2007; Heimsath et al., 1997) but these methods are invasive and typically fail to access to the deepest reaches of weathering, which may often extend many tens

of meters beneath the surface (e.g., Ruxton and Berry, 1957; Anderson et al., 2002; Buss et al., 2013). In contrast, application of geophysical techniques can non-invasively probe the deep subsurface and inexpensively quantify physical properties that reflect weathering and water storage over broad areas. For example, P-wave velocities, which can be readily measured in slope-spanning seismic refraction surveys, are influenced by mineralogy, porosity and density. Variations in these factors reflect variations in weathering with depth (e.g., Befus et al., 2011) and may also mark major subsurface boundaries, including the bedrock-regolith interface. Electrical resistivity, which can also be measured in slope-spanning surveys, is influenced by subsurface concentrations of water, dissolved salts (e.g., Saarenketo, 1998) and clay (e.g., Samouëlian et al., 2005), which reflect mass loss (and thus the opening of pores) and the degree of alteration due to subsurface weathering (Braun et al., 2009). Thus, when used separately or together, resistivity and seismic refraction surveys can put quantitative constraints on weathering and water-storage potential in landscapes (e.g., Beylich et al., 2003, 2004; Gallardo and Meju, 2003, 2004; Heincke et al., 2010; Olona et al., 2010; McClymont et al., 2011).

Here we present results of geophysical investigations of subsurface weathering and water-storage potential in the Southern Sierra Critical Zone Observatory (SSCZO), which is one of a growing network of multi-institutional, cross-disciplinary sites for long-term research on critical zone processes (Anderson et al., 2008). While geophysical studies of the near surface are increasingly common (e.g., Robinson et al., 2008; Knight et al., 2010), our work is the first of its kind at the SSCZO. Thus it provides a crucial dataset for understanding the role of subsurface weathering in ecosystem dynamics, landscape evolution, and the water cycle. Our work is unique in applying a rock physics model, based on Hertz-Mindlin contact theory, to quantitatively predict subsurface porosity distribution from seismic refraction velocities. We find that seismic velocity and electrical resistivity data are consistent with a weathering zone

5

that has an average thickness of 23 m along a transect spanning a heavily instrumented, forested slope and swampy meadow in the headwaters of one of the main SSCZO study catchments. Porosities from the rock physics model are as high as 50%, decreasing with depth (where velocities are higher) and assumed clay content in the model. Model-predicted porosities are broadly consistent with those measured from physical properties of saprolite. This suggests that our analysis of the geophysical data provides robust first-order constraints on subsurface weathering and water storage potential along the transect. Our results indicate that saprolite is a crucial reservoir of water, with capacity for up to 3 m^3/m^2 of water storage in the subsurface of a forested slope in the SSCZO. We couple our geophysical estimates of regolith thickness with erosion rates from previously published cosmogenic nuclide studies to put first-order constraints on the timescales of weathering in the landscape. We find that the soils at the surface reflect weathering and erosion averaged over hundreds of thousands of years, implying that they integrate over the wide fluctuations in climate associated with multiple interglacial-glacial intervals.

Setting

The SSCZO is located in Fresno County, California, USA, in granitic bedrock. It lies outside the limits of recent glaciation, in the heart of the so called "stepped topography" (Jessup et al., 2011; Wahrhaftig, 1965), a sequence of range-parallel ridges and valleys, with alternating steep and gentle terrain. Roadcuts in the area typically expose a sequence of saprolite overlying fresh granite. This suggests that variations in geophysical properties of the subsurface may often be straightforwardly interpreted to reflect variations in porosity and secondary mineral abundance.

120   The SSCZO lies within the Kings River Experimental Watershed (KREW), a site of long-

121   term research by the Pacific Southwest Research Station of the US Forest Service (Hunsaker and

122   Eagan, 2003). We focused on P301, one of three ~1 km² area CZO catchments at the head of

123   Providence Creek (Fig. 2a), which is part of the Kings River drainage. Vegetative cover, where

124   present, is dominated by a mixed-conifer forest consisting of white fir (*Abies concolor*),

125   ponderosa pine (*Pinus ponderosa*), Jeffrey pine (*Pinus jeffreyi*), black oak (*Quercus kelloggii*), sugar

126   pine (*Pinus lambertiana*) and incense cedar (*Calocedrus decurrens*), with minor cover by mixed

127   chaparral. Soils in the P301 have highly variable thickness (that is, depth to saprolite) but are

128   generally <1 m thick (Johnson et al., 2011). Cosmogenic nuclides in the top of saprolite on a

129   nearby slope yield soil production rates that range from 73 to 136 t km^{-2} yr^{-1} (Dixon et al., 2009).

130   Chemical erosion appears to account for ~40% (3) or more (Dixon et al., 2009) of overall

131   denudation (that is, physical plus chemical) at the site, and roughly half of all chemical erosion

132   occurs in saprolite (Riebe and Granger, 2013). Mean annual precipitation is approximately 1100

133   mm yr^{-1} (Hunsaker et al., 2012) and mean annual temperature is approximately 9 °C. The style

134   of precipitation varies from dominantly snow-derived in catchment headwaters to dominantly

135   rain-derived at the catchment mouths (Bales et al., 2011).

136   An improved understanding of the water balance at catchment scales is a major research

137   goal of the SSCZO (Anderson et al., 2008; Bales et al., 2011). Of particular interest are data and

138   analyses that help partition water fluxes into deep and shallow components. Another goal is to

139   explore implications of subsurface water flow and storage for the ecosystem, including

140   questions about the sources of water for vegetation and how they change throughout the year

141   (Lin et al., 2011). Observations of soil moisture, snow pack, and sap flow from a heavily

142   instrumented white fir tree (CZT-1) show that roughly one third of its annual

143   evapotranspiration is derived from depths > 1 m (Bales et al., 2011), suggesting that water

7

144 storage and through-flow in the deep subsurface may be a major component of the overall

145 water budget for the ecosystem. We use our geophysical measurements, described next, to

146 characterize the water storage capacity in the SSCZO at the hillslope scale.

147

148 **Acquisition and Processing of Data and Samples**

149 *Geophysical Survey Design*

150   Here we present data from two lines. Line 5 is a transect spanning a ridgetop, a forested

151 hillslope and an open meadow (Fig. 3), on which we acquired both seismic refraction and

152 electrical resistivity data. The transect crosses within 5 m of CZT-1 (Bales et al., 2011). The

153 survey is underlain by the Dinkey Creek pluton (Bateman and Wones, 1972), a fairly uniform,

154 medium-grained hornblende-biotite granodiorite, with abundant fist-sized (and smaller), disc-

155 shaped mafic inclusions. The second line (Line 9) was situated on a bare expanse of the Bald

156 Mountain pluton (Bateman and Wones, 1972), which is also medium grained, but devoid of

157 hornblende and mafic inclusions; this line was sampled to constrain velocities of what we refer

158 to as "unweathered" bedrock; though the surface exhibits minor alteration of biotite and

159 feldspar and modest fracturing and sheet jointing, it rings to the hammer and overall, appears

160 to be as fresh as rock gets at the surface in the area. Topography was surveyed on each line

161 using a tape measure and inclinometer; we estimate the accuracy in the surveyed positions to be

162 ±0.2 m (horizontally and vertically), which is sufficiently accurate for the geophysical methods

163 used here.

164

165 *Seismic Refraction Surveys and Tomographic Inversions*

166   We acquired seismic refraction data on Line 5 using two 24-channel Geometrics Geode

167 systems and 40 Hz vertical-component geophones spaced at 5 m, with a 12-pound

168 sledgehammer source striking a ~20 x 20 x 2 cm-thick stainless steel plate. In some instances we

169 supplemented data acquisition with 12-gauge shotgun blanks fired from a stainless-steel

170 muzzle implanted 1-2 meters deep in 5 cm-diameter auger holes. On Line 9, 24 geophones at 3

171 m spacing were attached to the outcrop using plaster of paris, and sledgehammer blows were

172 landed directly on the outcrop. Shot spacing was ~15 m on Line 5 and 6 m on Line 9.

173 We produced seismic velocity models using first-arrival, travel-time tomography. First

174 arrival times were picked manually on all traces with sufficient signal-to-noise ratios. An

175 example from each line is shown in Figure 3. Travel times were inverted for each line using

176 SeisImager© software as follows. First, an initial velocity model was generated by inserting a

177 uniform vertical velocity gradient (usually from 300 m/s to 4500 m/s) beneath the elevation

178 profile on the line. For the tomographic inversion, the model is discretized into cells of constant

179 velocity; cell dimensions were constant in the horizontal (3 m for Line 9 and 5 m for Line 5) and

180 varied in the vertical from about 2 m to 6 m. Rays were traced by the shortest path method

181 (Moser, 1991) from each shot to each receiver. The inversion was performed using an L2-norm

182 nonlinear least square algorithm, where the objective is to minimize the squares of the

183 differences between the measured and modeled first arrival travel time data. The inversion

184 typically results in smooth boundaries between regions with different velocity values. The

185 convergence criteria are based on reaching the maximum allowed number of iterations and/or

186 a user defined tolerance for the minimum change in root-mean-square error from one iteration

187 to the next. Ten iterations of a linearized least-squares inversion algorithm were conducted. No

188 horizontal or vertical smoothing to the velocity cells was applied during the inversion. Typical

189 agreement between predicted and observed travel times is shown in Figure 4. Agreement is

190 generally lower for longer travel times, which reflect information from the deepest parts of the

191 profile; here, ray coverage is lowest and thus provides least constraints on the inversion. The

9

192   deepest penetration by ray paths on Line 5 is ~40 m, dictated mostly by the overall length of the

193   geophone array in the survey.

194   Line 9 (Figure 4C) was acquired to identify the velocity that corresponds to relatively

195   unweathered rock exposed on an extensive outcrop. The data on Line 9 differ from those on

196   Line 5 in two important ways. First, at small source-receiver offsets, the first arrivals have

197   nearly linear slopes that indicate velocities of ~4.0 km/s at the surface (dashed line, Fig. 3B).

198   Second, the first arrivals have a high frequency content, with a center frequency around 400 Hz.

199   In contrast, data from Line 5 have much slower first-arrival velocities and a lower frequency

200   content, with a typical center frequency around 50 Hz. These characteristics are consistent with

201   a unweathered bedrock with a nearly uniform velocity of 4.0 km/s and low attenuation in the

202   subsurface (Fig. 4C). This observation, together with several lines of evidence presented later,

203   enables us to interpret velocities of 4.0 km/s in the subsurface of other lines, as "pristine"

204   bedrock.

205   In a linearized inversion, the final result can be highly dependent on the starting model.

206   The starting model must be realistic (that is, capture the velocity range of subsurface materials

207   at the survey site) in order for the inversion to converge to a realistic solution. Moreover, the

208   final result will often carry vestiges of the starting model. For example, a starting model that

209   consists of a simple linear increase in velocity with depth will generally produce a smoother

210   final model than a layered starting model, which will often lead to a final model that retains

211   sharp velocity increases where the original velocity steps were. We use a simple linear gradient

212   in velocity for our starting models in the absence of *a priori* knowledge of any sharp transitions

213   in velocity with depth.

214   Our tomographic inversion of seismic refraction data from Line 5 yields the velocity

215   model shown in Figure 5A. To quantify the sensitivity of the inversion to the initial velocity

10

216   model, we conducted a sensitivity analysis on Line 5. This involved fifty independent

217   inversions from a suite of starting velocity models, chosen based on the expected velocity range

218   of subsurface materials, wherein velocity increases linearly with depth from 0 to 50 m (Figure

219   6). Velocities at the surface and at 50 m depth were varied from 300 to 700 m/s, and from 3000

220   to 5300 m/s, respectively, resulting in a total velocity variation among starting models of about

221   800 m/s at 10 m depth, 1000 m/s at 20 m depth, and 1500 m/s at 30 m depth (Figure 6).

222   Velocity inversion parameters were held constant for all runs. The distribution of variance in

223   modeled velocities is shown both in terms of percent error and in standard deviation in Figure

224   6. Percent errors are typically ~5-10%, with velocity uncertainties of ±100 m/s in the upper 10 m

225   and ±300 m/s or more elsewhere. The sensitivity analysis suggests that our tomographic

226   inversion of Line 5 is not highly sensitive to variations in the starting model.

227

228   *Electrical Resistivity Measurements and Modeling*

229   Electricial resistivity tomography is commonly applied to image subsurface structures

230   with a detectable electrical resistivity contrast relative to the host medium. Because they are

231   sensitive to electrical conductivity (or, equivalently, resistivity) rather than elastic properties

232   (for example, velocity), electrical data can complement seismic refraction data in the

233   interpretation of CZ architecture. In particular, resistivity values can help distinguish between

234   two possible causes for increased seismic velocity: decreasing porosity (that is, less weathering)

235   or increasing saturation of the pore space (that is, the presence of water).

236   On Line 5 we acquired resistivity data using a 10-channel IRIS Instruments, Inc., Syscal

237   Pro 48©. To cover the entire transect, we spaced 48 stainless steel electrodes on the ground at 10

238   m intervals to create a 470-m-long line and used a dipole-dipole array with fixed 10 m spacing

239   between the current and voltage electrodes. To improve subsurface resolution, we added

11

240 measuring points by varying the distance between the current and voltage electrode pairs from

241 1 to 10 times the electrode spacing (i.e., 10-100 m). We acquired 710 measurements, with a

242 modeled maximum investigation depth of about 120 m based on theoretical relationships

243 between electrode spacing and geometry and investigation depth for a homogeneous earth

244 medium (e.g., Loke, 2004). Time constraints in the field prohibited reciprocal measurements.

245 Instead, we quantified noise levels using repeatability tests and edited data from Line 5 to

246 remove outliers and negative or zero apparent resistivity values. This reduced the dataset by

247 approximately twenty eight percent.

248   The objective of resistivity inversion is to find a resistivity model that provides a set of

249 theoretical measurements (forward response) that fit the measured data to some pre-described

250 acceptable level (e.g., LaBrecque and Ward, 1990; Oldenburg and Li, 1999; Loke et al., 2003;

251 Günther et al., 2006). If *a priori* information about the subsurface is unavailable, then a

252 smoothness-constraint inversion is utilized to produce smooth models. However, this

253 regularization constraint is conceptually inappropriate when the depths of sharp resistivity

254 contrasts are desired, as is the case here, where quantifying the depth to highly resistive, fresh

255 bedrock is a goal. If *a priori* subsurface data from geological logs or other geophysical methods

256 are available, alternatives to smoothness-constraint inversion may be used to define layers with

257 sharply contrasting resistivity. For example, in disconnect inversion (Slater and Binley, 2006),

258 the inversion solves for a smoothly varying model structure above and below the resistivity

259 boundary (that is, the "disconnect") without smoothing across it.

260   We inverted Line 5 data using both a standard smoothness-constraint inversion and a

261 disconnect inversion approach using DC2DInvRes (Günther, 2005). The convergence criterion

262 is based on the assumption that the normalized χ^2 equals 1 if the data are appropriately

263   weighted given the actual noise and data noise is normally distributed (Johnson et al., 2012),

264   where χ^2 is calculated using Equation 1.

$$\chi^2 = \frac{1}{N_d - 1} \sum_{i=1}^{N_d} \left(\frac{d_{pred,i} - d_{obs,i}}{\sigma_i} \right)^2 \qquad (1)$$

265   Here N_d is the number of measurements, dpred is the predicted data, dobs is the

266   measured data, and σ_i is the standard deviation of the measured data. In our inversions, χ^2

267   equals 1 when we assume that the data are contaminated with 4% noise. The discretized model

268   space of the foreground region (that is, the area encompassed by the electrode array) contains

269   2350 cells (a 94 by 25 mesh). We set horizontal cell dimensions at 5 m, equal to one half the

270   electrode spacing, whereas vertical dimensions of cells varied logarithmically from 0 to 130 m.

271   To assess how well our model cells are controlled by the measured data as opposed to model

272   constraints, the sum of absolute sensitivities of all data points are combined and displayed in

273   Figure 7A (following Günther et al., 2003). The results of the sensitivity analysis indicate that

274   the maximum depth of investigation at which the model cells are controlled by the data is about

275   90 m. As expected, the sensitivities are very low near the model boundaries. To explore this

276   more, we inverted Line 5 data using two different homogenous initial models of 2000 ohm-m

277   and 5000 ohm-m. The resulting models show consistent spatial distributions of resistivity

278   within the subsurface up to a depth of 90 m, particularly in the high resistivity zone (Figure 7B

279   and 7C).

280   Figure 8A shows the result of inverting the Line 5 data using the smoothness-constraint

281   inversion method. The inverted model displays a wide range of resistivity values. Resistivity

282   ranges from 500 to 25k ohm-m and is generally higher (> 104 ohm-m) beneath the ridge on the

283   south side of the profile than beneath the swampy meadow to the north (<104 ohm-m). As

284   expected, due to the effects of using the smoothness constraint, the high and low resistivity

285   zones within the model space have smeared boundaries, which make it difficult to decide if

286   those boundaries are real or simply a result of the employed inversion approach. Regolith with

287   low resistivity is relatively thin (10 m or less) on the hillslope and thickens abruptly to > 30 m

288   near the base of the hill and stays deep throughout the meadow, where the upper ~ 40 m is

289   marked by low resistivity values and strong lateral variations. Generally, the inferred seismic

290   velocity contours (Figure 5A) follow the lateral changes in resistivity, particularly beneath the

291   ridge. However, since the smoothness-based inversion smears out layer boundaries, accurate

292   comparison between the two physical properties (that is, velocity vs. resistivity) across the

293   model space is not reliable. To obtain a simplified model (with few resistivity structures) based

294   on Figure 8A, we performed hierarchical clustering, which is based on the magnitude,

295   horizontal location and depth of each model cell (e.g., Defays, 1977; Günther, 2005). The cluster

296   analysis indicates that the model space consists of four clusters, each having different resistivity

297   value (Figure 8B). The high resistivity zone beneath the ridge is portioned into two clusters, a

298   result which fits fairly well with the seismic contours at this location. On the other hand, the

299   meadow area is portioned into three clusters with different geometries. Unlike under the ridge,

300   the velocity contours under the meadow do not always closely follow inferred resistivity

301   changes.

302   To obtain an improved estimate of the resistivity distribution above and below the fresh

303   granite bedrock, we inverted the data using the disconnect-inversion approach by incorporating

304   a boundary in the regularization based on the 4 km/s velocity contour. The disconnect-

305   inversion yields somewhat sharper resistivity boundaries (Figure 8C vs. Figure 8A) and an

306   improved match between the seismic contours and the resistivity boundaries, especially

307   beneath the meadow, where the low-resistivity body (~900 ohm-m) is bounded at its base by

308   the 4 km/s velocity contour. The cluster analysis for the disconnect-inversion model (Figure 7d)

14

309 shows that the resistivity data can be roughly fit (39% RMS error) with only a few major bodies,

310 including (1) a core of high resistivity (~19,000 ohm-m) that lies mostly beneath the 4 km/s

311 contour beneath the hilltop and slope, (2) a surrounding rim of moderately high resistivity

312 (~7,000 ohm-m), and (3) relatively low-resistivity (~900 ohm-m) bodies that extend from the

313 shallow portions of the hillslope to 30 m beneath the meadow. The RMS data misfits for the

314 smoothness-constraint inversion and its associated cluster analysis are 8.4% and 36.8%,

315 respectively. Similarly, RMS misfits are 8.3% and 39.2% for the disconnect inversion and its

316 associated cluster analysis. The forward response of the inverted models fits well with the

317 observed data except at few spots that have low data coverage (Figure 9). As expected, the

318 cluster analyses models have higher RMS data error than the smooth and disconnect inversion

319 approach, since the model space is constrained to a few model parameters, limiting the

320 minimization of data misfit.

321 For the purposes of comparison to the seismic model and geological interpretation,

322 discussed later in the paper, we use the disconnect model of Fig. 7c as our preferred model.

323

324 *Bulk Density and Porosity*

325 To put additional constraints on variations in subsurface weathering across the site, we

326 measured saprolite porosity (φ), that is, its volumetric water-storage capacity, on samples

327 collected using both hand augers and Geoprobe coring. Hand auger samples were collected

328 from depths of 30 to 540 cm by augering into saprolite at five locations within a 5 m radius of

329 CZT-1, located near the crest of the ridge spanned by Line 5 (Fig. 2B and Table 1). We also

330 augered into the subsurface and collected samples at two additional points along Line 5.

331 Together, our regolith samples provide an independent check on geophysics-based estimates of

332 subsurface porosity (as discussed later). All samples were collected coincident with the

333 geophysical surveys, in September and October, 2011. At each point, we first hand augered a

334 hole to just above the target sampling depth, and then drove a cylinder of known volume into

335 the underlying saprolite using a slide-hammer attachment on either a Madera© sampler (for

336 shallow depths) or an AMS© sampler (for deeper depths). To minimize compaction that might

337 be induced by the hammer, we used marks on the sampler as a gauge on when to stop driving

338 the cylinder.

339   In September 2012, additional volumetric soil samples were collected from five boreholes

340 along the geophysical transect down to a maximum depth of 11.5 m, using a Geoprobe 6610DT,

341 direct push dual speed auger. Samples were collected and sealed in the field in clear plastic

342 sleeves. One-meter core sections were augured at a time and each core was labeled and logged

343 in the field for visual changes in soil type and water content. The core sections were sealed in

344 the field with vinyl end caps and parafilm to prevent moisture loss. In the lab, each one meter

345 section was sub-sampled in 10 cm increments. Volumetric samples were weighed in the lab and

346 placed in an oven to dry for a 24 hour period at 105 °C (Flint and Flint, 2002). After 24 hours,

347 the samples were weighed to obtain an accurate dry soil mass for calculation of the samples'

348 bulk density (ρ_b) and volumetric water content. While use of the Geoprobe limits the sample

349 compaction, the use of the hammer, especially at shallow depths, can lead to some compaction.

350 Measured bulk density was corrected for compaction based on the amount of core recovered

351 per one meter pushed. The maximum depth was determined by the rejection depth of the

352 Geoprobe. Here we use samples from hole CZG-1, which was located near the ridge at tree

353 CZT-1.

354   Porosity of both hand-auger and Geoprobe samples was estimated as

355
$$\varphi = 1 - {\rho_b}/{\rho_s} \qquad\qquad (2)$$

16

356   where ρ_s is the particle density, here assumed to be 2.65 g cm^{-3} (Flint and Flint, 2002). We

357   measured the mass of each sample in both the field and laboratory before oven drying them for

358   24 hours at 105 °C (Flint and Flint, 2002). We weighed the samples again after allowing samples

359   to cool (thus minimizing effects of convection) for estimates of dry soil mass, which in turn

360   enables calculation of bulk density (based on the known cylinder volume), used here in

361   Equation 2 to estimate porosity. Saturation, the percent of pore volume occupied by water, was

362   calculated as the volumetric water content divided by porosity. Results for our porosity

363   measurements are shown in Table 1. Porosity ranges from 0.35 to 0.64, with higher values

364   generally near the surface.

365

366   **Discussion**

367   *Weathering timescales*

368   The geophysical estimates of regolith thickness from Line 5 range from ~10 to 35 m (Fig.

369   5c). How long does it take to develop a weathering profile that thick? Or, more appropriately,

370   given that the regolith is eroding, what is the average residence time of regolith on the

371   landscape? To find out, we simply divide regolith thickness by an estimate of its overall erosion

372   rate, or equivalently (assuming steady-state thickness), by the regolith production rate.

373   Although regolith production rates are not easy to measure (Dosseto et al., 2008), cosmogenic

374   nuclides average erosion rates over millennial timescales and thus can be used to roughly

375   approximate regolith residence times. In situ-produced cosmogenic [10]Be in saprolite from a

376   slope on the edge of P301 (Dixon et al., 2009) yield the most proximal estimate for our purposes.

377   The overall denudation rate (including both chemical and physical erosion) for the slope is

378   reportedly 220 t km^{-2} yr^{-1} (Dixon et al., 2009), near the middle of the factor of ~10 range of

379   denudation rates implied by cosmogenic nuclides in stream sediment from elsewhere in the

17

380 Sierra Nevada (Riebe et al., 2000; Riebe et al., 2004). It is also broadly consistent with the ~0.3 m

381 Ma^{-1} regional average rate of river incision (equivalent ~80 t km^{-2} yr^{-1} of landscape erosion),

382 which has evidently persisted for the last ~1 Ma, according to cosmogenic burial dating of cave

383 sediment in the region (Stock et al., 2004).

384   To obtain regolith residence times, we first convert thickness to mass using the average

385 density of subsurface samples reported in Table 1 (i.e., ~1.40 g cm^{-3}). We then divide the range

386 in masses by the erosion rate (220 t km^{-2} yr^{-1}) and calculate 64 – 220 ka as a plausible range of

387 regolith residence times. Thus soils found at the surface today in the SSCZO evidently reflect

388 the integration of subsurface weathering and erosion over 10^5-year timescales. This suggests

389 that regolith properties and structure we see in our geophysical surveys may be relics of past

390 conditions that were very different from those that drive weathering and erosion today.

391 Although incision rates of master drainages in the region have apparently been fairly stable

392 over the estimated range of residence times (Stock et al., 2004), the streams surrounding the

393 SSCZO are marked by pronounced knickpoints (Wahrhaftig, 1965), consistent with waves of

394 incision propagating through the landscape. Even if base-level lowering rates have been

395 roughly steady, climate has fluctuated markedly in the region over the last 100 – 200 ka (e.g.,

396 Oster et al., 2009). Although the SSCZO lies outside of the mapped limits of Pleistocene

397 glaciation (Gillespie and Zehfuss, 2004), it is high enough that it was likely influenced during

398 glacial intervals by periglacial processes, which could have affected erosion and subsurface

399 weathering. In addition, any variations in temperature and moisture over time might have

400 influenced the instantaneous weathering rate; one implication of this may be that long-term

401 averages measured by geochemical mass-balance techniques (e.g., Riebe et al., 2004; Dixon et

402 al., 2009; Rasmussen et al., 2011) do not strongly reflect effects of current climatic conditions.

403   The long residence times and possible influence of climate change on regolith at the

404   SSCZO raise doubts about whether outputs from erosion are balanced by inputs from regolith

405   production (Fig. 1) over the timescales of regolith formation. If not, then the thickness and

406   possibly also properties of regolith have been changing and the system is not in geomorphic

407   steady state. Similar doubts surfaced in an intensive study of subsurface well logs and

408   cosmogenic nuclides in granites of the Colorado Front Range (Dethier and Lazarus, 2006), in

409   what is now the Boulder Creek CZO. In contrast, at the Luquillo CZO, in tropical Puerto Rico,

410   the consistency among rates of weathering and erosion over diverse timescales (White et al.,

411   1998; Riebe et al., 2003; Buss et al., 2008; Ferrier et al., 2010) has been interpreted to imply that

412   regolith developed in quartz diorite bedrock is in geomorphic steady state (Chabaux et al.,

413   2013).

414

415   *Porosity in saprolite*

416   Seismic velocity in saprolite is lower than in unweathered granite for two reasons:

417   increased porosity due to weathering, and the replacement of minerals such as feldspars with

418   lower-velocity clays (e.g., Olona et al., 2010). We can estimate the porosity distribution in the

419   subsurface from our seismic velocity models by predicting the velocity of a mineral aggregate

420   over a range of possible porosities and finding the porosities that best match the observed

421   velocities. Since modeled porosity depends on the saturation state of the pores, we calculate

422   two end-member estimates of porosity, one for dry porosity and one for saturated. The dry

423   porosity model provides a minimum estimate of porosity, since fully saturated rocks have

424   higher velocities than dry rocks and thus a higher potential porosity than dry rocks of equal

425   velocity (e.g., Mavko and Mukerji, 1998). We then compare our predicted porosity models to

426   porosity and saturation values measured on the auger and Geoprobe core samples near CZT-1.

19

427 As will be seen below, the core samples match the minimum (dry)-porosity model in the upper

428 few meters of the subsurface and approach the saturated-porosity model near the base of the

429 saprolite (~10 m).

430   We predict seismic velocity as a function of porosity and mineralogy with a rock physics

431 model based on Hertz-Mindlin contact theory (Mindlin, 1949), as formulated by Helgerud

432 (2001) and Helgerud et al. (1999). This approach treats regolith and rock as aggregates of

433 randomly packed spherical grains and expresses their bulk elastic properties (bulk modulus, K,

434 and shear modulus, G) as functions of effective pressure, porosity, the elastic properties of

435 constituent minerals, and a critical porosity (φ_c) above which the aggregate changes from a

436 suspension to a grain-supported material (typically 36-40%; (Nur et al., 1998)). The Hertz-

437 Mindlin theory establishes the effective bulk (K_{HM}) and shear (G_{HM}) moduli of the dry rock

438 frame at φ_c as

439

440
$$K_{HM} = \left[\frac{n^2(1-\varphi_c)^2 G^2}{18\pi^2(1-\nu)^2} P_{eff} \right]^{1/3} \qquad (3)$$

441
$$G_{HM} = \frac{5-4\nu}{5(2-\nu)} \left[\frac{3n^2(1-\varphi_c)^2 G^2}{2\pi^2(1-\nu)^2} P_{eff} \right]^{1/3} \qquad (4)$$

442

443 where ν is Poisson's ratio, $(3K-2G)/(6K+2G)$, n is the average number of contacts per grain (we

444 use n=5, following Bachrach et al., 2000), and effective pressure, P_{eff}, is given by

445
$$P_{eff} = (\rho_b - \rho_w)gD \qquad (5)$$

446

447 In equation 5, ρ_w is the density of water (1000 kg/m³), D is the depth below the surface in

448 meters, g is gravitational acceleration (9.8 m/s²), and ρ_b is the bulk density, given by

$$\rho_b = \varphi \rho_w + (1 - \varphi)\rho_s \tag{6}$$

where ρ_s is the density of the solid mineral constituents (here taken as 2650 kg/m³). We assume a φ_c of 0.38 and use the modified upper and lower Hashin-Shtrikman bounds (equations 6.4-6.7 of Helgerud, 2001), respectively, to calculate elastic moduli of the dry frame (K_{dry} and G_{dry}) above and below φ_c. Once the bulk and shear moduli (K and G) of the medium for a given porosity are calculated, P-wave velocity can be calculated from

$$v_p = \sqrt{\frac{K + \frac{4}{3}G}{\rho_b}} \tag{7}$$

The rock physics model presented above must be applied differently for dry (air-filled) or saturated (water-filled) porosity, as K, G and ρ_b in equation 7 depend on the pore fluid. To model dry porosity, we set ρ_w=0 in equations 5 and 6, since air has a density of ~0 and the effective pressure for dry saturation depends only on the bulk density of the overlying solid material, and use K_{dry} and G_{dry} as K and G in equation 7. For saturated porosity, the bulk modulus is given instead by K_{sat}, calculated from Gassmann's (1951) equation:

$$K_{sat} = K_{solid}\frac{\varphi K_{dry} - \frac{(1-\varphi)K_f K_{dry}}{K_{solid}} + K_f}{(1-\varphi)K_f + \varphi K_{solid} - K_f K_{dry}/K_{solid}} \tag{9}$$

We tested the sensitivity of our predicted velocities (and thus porosities) to compositional variations by modeling the elastic properties of the solid frame over a range of 25-50% quartz (K=44 GPa, G=36.6), 10-65% feldspar (K=70 GPa, G=30 GPa), and 0-65% clay (K=20.9 GPa, G=6.85 GPa), which simulates effects of a large range in degree of weathering of feldspars to clays (elastic constants from Helgerud et al. (1999) and Bass (1995)). These minerals typically

21

470 dominate regolith in granite weathering profiles (Dahlgren et al., 1997); variations in the

471 abundance of other primary and secondary minerals (for example, hornblende) will not

472 significantly affect the predicted velocities. Bulk solid elastic constants were calculated using

473 the averaging formula of Hill (1952). We create a porosity model by varying porosity in

474 Equation 6 to predict velocities from Equation 7, then comparing with the tomographic velocity

475 model to find the best-fitting porosity at each point in the subsurface.

476   A minimum (dry)-porosity model calculated in this way, assuming a mineralogy of 50%

477 feldspar, 25% quartz, and 25% clay, shows that substantial porosity exists in the saprolite

478 beneath much the surface on Line 5 (Figure 10B), consistent with weathering that is both

479 extensive and deep. Predicted porosities are about 0.4±0.1 at the surface, decreasing with depth

480 to zero at around 25-30 m depth (shallower in places). On average beneath the hillslope,

481 minimum porosity is 0.2 or higher in the upper ~8 m. Subsurface weathering at the hilltop

482 around the heavily instrumented white fir (CZT-1) is particularly extensive and deep, with

483 minimum porosities of 0.2 extending down to about 10 m depth and 0.05 down to 15 m depth.

484 Uncertainties in modeled porosity due to potential mineralogical variability are about ±0.1 at

485 the surface and decline substantially with depth. We note that the predicted velocity at zero

486 porosity for compositions considered here is about 4.2 km/s, close to the 4.0 km/s observed on

487 the granite outcrop; this suggests that our porosity model is calibrated to within ±0.05, at least at

488 the low-porosity end.

489   Samples of saprolite from hand augering and Geoprobe coring near CZT-1 provide an

490 important check on our porosity model and indicate the critical role of pore saturation in

491 creating porosity models from seismic velocities. Measured porosity values in the upper few

492 meters are high (~40-50%), consistent with porosities predicted by our minimum-porosity

493 model (Figure 10). However, at depths greater than ~3 m, sample porosities diverge from the

494 model, staying well above the minimum-porosity model down to depths of 10 m. The

495 explanation for this lies in the observed saturation values of the samples, which increase from

496 ~15-20% in the upper 2 m to nearly ~90% at 10 m depth (Table 1). As saturation increases with

497 depth, the observed porosity values approach the saturated-porosity model, as expected (Fig.

498 9B). This comparison indicates that our minimum-porosity model produces reasonable

499 estimates where pore space is dry but may significantly underestimate total porosity in water-

500 saturated settings.

501

502 *Comparison of Seismic Velocity and Resistivity*

503 Because seismic velocity and resistivity are sensitive to different physical properties, a

504 comparison between them can enhance insight into subsurface structure and water content

505 (Figure 8). Here we compare the resistivity model obtained from the disconnect-inversion

506 approach with the seismic velocity model, as this approach is conceptually consistent with the

507 expected resistivity transition from regolith to unweathered bedrock. High resistivities (>10^4

508 ohm-m) reach the surface just south of the hilltop, where bedrock crops out, consistent with the

509 expected high resistivity of granite (>10^4 ohm-m; (Olhoeft, 1981)). Velocities there are nearly 2

510 km/s at the surface. The underlying 4 km/s contour, which likely marks the transition from

511 moderately to unweathered bedrock (as described below) approximately follows the transition

512 between moderate (~7,000 ohm-m) and high (~19,000 ohm-m) resistivities. Beneath the upper

513 hillslope (x=70-150 m), the upper ~15 m of the subsurface has velocities <2.0 km/s (probably

514 encompassing saprolite, as discussed below) and lower resistivity values (<10^3 ohm-m) that

515 likely indicate the presence of clay and/or small amounts of water.

516 Several zones of low resistivity (<1000 ohm-m) exist in the model beneath the hillslope

517 and meadow. The lowest resistivities (<600 ohm-m) form a northward-dipping, highly

23

518   conductive body in the uppermost 5-10 m beneath the meadow (x=220-270 m in Fig. 8).

519   Resistivity in rocks and soils is strongly dependent on porosity, pore saturation and pore fluid

520   content, as water is typically much less resistive than minerals (e.g., Samouëlian et al., 2005);

521   electrical conductivity due to water in soils increases rapidly as saturation increases from

522   adsorbed water in the vadose zone to free water in pores (e.g., Saarenketo, 1998). The

523   conductive body in the meadow very likely corresponds to the water table; the meadow itself

524   was water-logged and marshy at the surface during the survey. Alternatively (or additionally),

525   low resistivity could indicate the presence of clays, which enhance conductivity (Samouëlian et

526   al., 2005). Whether the low-resistivity bodies indicate the presence of water or clay (or both),

527   they are likely linked to coupled weathering and hydrological processes, since water is a major

528   agent for bedrock weathering. In the disconnect inversion, the 4 km/s contour corresponds

529   nearly everywhere to a downward increase in resistivity, consistent with an interpretation of

530   that velocity value marking the transition from weathered to nearly intact bedrock. The one

531   exception is a deeper pocket of low resistivity just beneath 4 km/s contour under the southern

532   edge of the meadow (x~200 m), possibly indicating a locally saturated zone within the bedrock.

533   All inversion results show a strong lateral change in bedrock resistivity beneath the 4

534   km/s contour, from highly resistive rock (~19,000 ohm-m) beneath the upper hillslope to much

535   less resistive (~2,000 ohm-m) beneath the lower hillslope and meadow (for example, the

536   transition from units I to II to IV in Fig. 8D). The most likely explanation for this change is a

537   contrast in the saturation of pore spaces (microporosity and/or fracture porosity) in the

538   bedrock, from dry porosity at the top of the hillslope to saturated conditions beneath the lower

539   hillslope and meadow. Alternatively the phenomenon could reflect precipitation of clays in the

540   meadow from leaching of regolith on the slope (e.g., Yoo et al., 2009). The downslope

541   enrichment of clay would appear as a decrease in resistivity, which might be abrupt -- at the

542 forest-meadow transition -- if illuviation is driven by reducing conditions associated with the

543 more continuous presence of water in the meadow. The corresponding change in seismic

544 velocities might be less pronounced due to their lower sensitivity to clay content (Fig. 10).

545 Drilling and sampling of the subsurface in the region near the meadow would help test this

546 hypothesis.

547

548 *Conceptual Model*

549 The coupled seismic and resistivity data presented here offer unique insights into the

550 subsurface structure and water content of the SSCZO and thus provide a basis for generating a

551 conceptual model of the critical zone (Fig. 11). The model has two main features relating to

552 weathering (primarily inferred from seismic velocities and porosities) and pore saturation

553 (primarily inferred from resistivity values). First, a vertically stratified weathering profile is

554 indicated by the increasing seismic velocities (and inferred porosity decrease) with depth.

555 Beneath a thin soil layer (which is assumed but not resolved in our geophysical images), we

556 interpret three main subsurface layers: saprolite, moderately weathered bedrock, and

557 unweathered bedrock. Second, a lateral change in pore saturation (and/or clay content) is

558 suggested by the strong lateral change in resistivity from the hillslope to the meadow. Below

559 we describe the basis for the interpretive cross-section (Fig. 11) in detail.

560 Saprolite is defined here as the sub-soil unit where velocities are less than 2 km/s.

561 Beneath the hillslope on our model, the 2 km/s contour closely coincides with a major

562 downward increase in resistivity, from <1,000 ohm-m to >5,000 ohm-m, suggesting that, in the

563 relatively "dry" (electrically resistive) hillslope environment, the 2 km/s contour marks a

564 significant physical transition. The porosity model (Fig. 10) provides further support for this

565 interpretation: at the depths with V=2 km/s, (~20 m at x=50 m) porosity is only 5-10%, much

566 lower than typical saprolite porosities (>20%, e.g., Driese et al., 2001). Several previous studies

567 of velocities in weathered granite terrains support choosing the 2 km/s contour as a threshold

568 between saprolite and moderately weathered bedrock (Begonha and Braga, 2002; Olona et al.,

569 2010). Begonha and Braga (2002) measured seismic velocities on weathered granite and

570 saprolite samples from the Oporto granite (Portugal) and found a close correlation between the

571 degree of weathering, seismic velocity and porosity and identified porosity as the physical

572 property most strongly influenced by weathering. They measured ultrasonic velocities on 167

573 drill core samples; 2.0 km/s marks the boundary between samples characterized as weathering

574 grade W3 ("weathered rock") and W3-W4, which includes saprolite. Olona et al. (2010)

575 conducted a comprehensive study of the elastic (Vp, Vs) and electrical properties of a

576 weathering granite terrain in northwest Spain. Their study included ground-truthing from a 35-

577 m-deep borehole and laboratory measurements of density, porosity, and ultrasonic velocity.

578 The boundary between granite "fully or partially weathered to soil," with a rock quality

579 designation (i.e., RQD after Deere, 1964) of 17%, and "fresh rock," with an RQD of >50%,

580 corresponds to an increase in P-velocity from 1.45 km/s to 2.6 km/s. These lines of evidence all

581 point to 2 km/s as a good proxy for the boundary between saprolite and underlying moderately

582 weathered bedrock.

583   The transition from moderately weathered to virtually intact basement likely takes place

584 near the 4 km/s isovelocity contour. Several lines of evidence support this interpretation. First,

585 seismic data from Line 9 (Figs. 2-5) show that intact bedrock exposed in an extensive surface

586 outcrop has a seismic velocity of 4 km/s. While this bedrock is not pristine -- it shows several

587 macroscopic fractures and some biotite staining -- it is intact and shows only slight weathering.

588 This outcrop thus provides direct "ground truth" that 4 km/s corresponds to only virtually

589 unweathered bedrock in our study area. Second, the rock physics model presented above

590 predicts a velocity of 4.2 km/s for zero porosity at the low confining pressures of our study area

591 under the mineralogies assumed here. Hence, a velocity of 4.0 km/s indicates, on average, low

592 porosities (<0.01), consistent with only slightly weathered bedrock. (In some places, low

593 resistivity zones beneath the 4.0 km/s contour may indicate local, fluid-filled fracture zones that

594 are too narrow to resolve with traveltime tomography.) Finally, comparison to other seismic

595 and borehole studies of weathering granite terrains indicates that 4.0 km/s corresponds to

596 slightly weathered (Begonha and Braga, 2002) or "fresh" rock (Olona et al., 2010).

597 The conceptual model in Figure 11 provides a glimpse of the thicknesses of saprolite and

598 weathered bedrock in the SSCZO. The thickness of regolith (defined for our purposes as the soil

599 plus saprolite plus moderately weathered bedrock) ranges from ~10 to 35 m (average = 23 m),

600 with the thickest regolith on the ridge (beneath CZT-1) and the thinnest regolith at the base of

601 the hillslope, just south of the swampy meadow. Meanwhile, saprolite thickness ranges from

602 near zero at the base of the hillslope to about 20 m near CZT-1. These thicknesses are broadly

603 consistent with studies of saprolite development elsewhere in granites of the southern Sierra

604 Nevada (Graham et al., 2010) and with our own general observations of weathering profiles in

605 roadcuts in the region.

606 At the north end of the seismic and resistivity surveys on Line 5, a blocky bedrock

607 outcrop was crossed ("fractured bedrock," FB, in the interpretive cross-section; Fig. 11). The

608 granite there appears as a resistive block on the resistivity model (x=270-310 m, Fig. 8), but the

609 surface layer of the seismic velocity model there shows low velocities (<1000 m/s). The low

610 seismic velocities here (which are resolved by travel times recorded by the end shotpoint; Fig. 4)

611 must therefore indicate that pervasive fracturing of the surface bedrock has lowered seismic

612 velocities to be indistinguishable from saprolite. Alternatively, the block of rock, while evident

613 at the surface, may be too small to be fully resolved as a 4 km/s anomaly by the seismic survey.

614   The high resistivity of this zone suggests that the fracture porosity was unsaturated, consistent

615   with drainage of residual moisture from the slope by the time of our survey, in October (that is,

616   long after the last of the previous winter's snow melted from the site).

617   Our conceptual model includes speculations on possible subsurface water flow paths

618   (arrows, Fig. 11). In hard rock terrains, weathering exerts a major control on hydrogeology.

619   Porosity is primarily a function of degree of weathering (e.g., Begonha and Braga, 2002),

620   whereas connectivity and permeability are affected both by porosity and by hydraulic

621   conductivity along fissures (Dewandel et al., 2006; Taylor and Howard, 2000). Permeability is

622   likely to be anisotropic in the presence of fractures (Marechal et al., 2003); significant hydraulic

623   conductivity can persist in weathered granite terrain to depths of 35 m, due to intersecting sets

624   of sub-horizontal and sub-vertical fractures (Marechal et al., 2004).   We speculate that

625   subsurface water flow is largely downhill from the vicinity of CZT-1, which was largely dry at

626   the time of our survey, based on resistivity measurements, to the meadow, which was saturated

627   and boggy during our survey, with the water table at the surface. Downslope flow is guided by

628   permeability structure and orientation of weathering zones. In particular, the downslope dip of

629   the base of the saprolite (Fig. 11) likely channels flow down toward the meadow. The stark

630   resistivity contrast between the resistive hilltop and more conductive lower meadow may be a

631   permeability phenomenon; we speculate that gravity-driven drainage precludes percolation of

632   water into the low-porosity, weathered bedrock beneath the slope, whereas low hydraulic

633   gradients and ponding in the meadow may permit water to seep more effectively into bedrock

634   cracks. We speculate that the isolated highly conductive zones beneath the meadow may

635   represent areas of recharge or ponding of subsurface water, with possible contributions from

636   conductive clays that precipitate there as by-products of illuviation from weathering upslope.

637　Such conductive bodies may hold important clues about subsurface weathering patterns in the

638　landscape.

639　　　There are numerous caveats to the physical, geochemical and hydrological

640　interpretations presented above. First, it is important to keep in mind that the boundaries

641　between layers are likely not sharp; weathering profiles are probably gradational in nature, and

642　while sharp fronts may exist in places, the simple structure shown in Figure 11, with sharp

643　boundaries between "moderately" and unweathered bedrock, or between saprolite and

644　weathered bedrock, is certainly a simplification. Second, our seismic velocity models, like all

645　tomograms, must be viewed as a spatially smoothed version of reality (e.g., Rawlinson et al.,

646　2010). This smoothing is due to limitations in ray coverage, regularization of the inversion

647　algorithm, and seismic wavelength (20 m for a 100 Hz wave traveling at 2000 m/s). As a

648　consequence, we are unable to distinguish between relatively intact corestones and surrounding

649　highly weathered zones, and our tomogram is an average velocity structure that blurs these

650　distinctions. The fractured bedrock (FB) interpreted on Figure 11 is a direct example of the

651　difficulty in distinguishing macroporosity due to fracturing from microporosity due to

652　weathering; similar regions of fractured bedrock in the subsurface could easily be mistaken for

653　saprolite in the seismic models. Third, we lack data on hydraulic head in this watershed, so our

654　suggestions of possible subsurface groundwater flow are purely speculative. While hydraulic

655　head is generally expected to mimic topography, with recharge zones at high elevation and

656　discharge at lower elevation, this may not be true in any given catchment (Winter, 1999).

657　Finally, and most importantly, our geological interpretation is unconstrained by direct sampling

658　via boreholes or outcrops. Nevertheless, we should be able to test the interpretation proposed

659　by Figure 11 in future drilling, sampling, and hydrogeological measurements. The competing

660　hypotheses proposed here arise from the coupling of resistivity and seismic refraction studies;

29

661   this highlights a benefit of using multiple geophysical approaches in the study of deep CZ

662   architecture and processes.

663

664   **Conclusions**

665   We investigated the subsurface architecture of the Southern Sierra Critical Zone

666   Observatory using seismic refraction and electrical resistivity data. Seismic velocity variations

667   provide robust first-order constraints on the distribution of weathering in the subsurface. We

668   find depths of weathering average about 23 m, consistent with roadcuts and other regional

669   studies of deep weathering. Beneath a roughly meter-thick layer of soil, regolith is divided

670   approximately equally between an upper layer of saprolite and a lower layer of moderately

671   weathered bedrock. We couple our geophysical estimates of regolith thickness with previously

672   published long-term erosion rates and infer that soils now found at the surface integrate

673   weathering over 100,000-year timescales and thus may reflect the influence of wide fluctuations

674   in climate associated with multiple glacial-interglacial intervals.

675   We used a rock physics model based on Hertz-Mindlin contact theory to constrain water

676   storage potential in the subsurface. Porosities predicted from a minimum-porosity model

677   decrease from ~50% near the surface to near zero at the base of weathered rock and are broadly

678   consistent with physical measurements of porosity in samples from the upper 3 m of the

679   subsurface. Porosities measured in deeper (3-10 m) samples are higher than those predicted by

680   the minimum-porosity model and approach the predicted values of a water-saturated porosity

681   model, consistent with their observed increasing saturation. These results indicate that seismic

682   velocities can be used to estimate minimum water storage potential in the subsurface. Across

683   the surveyed slope, we estimate that the minimum water storage potential averages ~3 m^3/m^2

684   of water and ranges from <1 to 5 m^3/m^2. Our results imply that saprolite and weathered

685   bedrock of the deep CZ may be crucial water storage elements in the SSCZO.

686

References

Anderson, S. P., W. E. Dietrich, and G. H. Brimhall (2002), Weathering profiles, mass-balance analysis, and rates of solute loss: Linkages between weathering and erosion in a small, steep catchment, Geological Society of America Bulletin, 114, 1143.

Anderson, S. P., F. von Blanckenburg, and A. F. White (2007), Physical and chemical controls on the Critical Zone, Elements, 3, 10.2113/gselements.3.5.315, 315-319.

Anderson, S. P., R. C. Bales, and C. J. Duffy (2008), Critical Zone Observatories: Building a network to advance interdisciplinary study of Earth surface processes, Mineralogical Magazine, 72, 10.1180/minmag.2008.072.1.7, 7-10.

Anderson, R. S., S. P. Anderson, and G. E. Tucker (2013), Rock damage and regolith transport by frost: an example of climate modulation of the geomorphology of the critical zone, *Earth Surf. Process. Landf.*, *38*(3), 299-316.

Bachrach, R., J. Dvorkin, and A. M. Nur (2000), Seismic velocities and Poisson's ratio of shallow unconsolidated sands, Geophysics, 65(2), 559-564.

Bales, R. C., J. W. Hopmans, A. T. O'Geen, M. Meadows, P. C. Hartsough, P. Kirchner, C. T. Hunsaker, and D. Beaudette (2011), Soil Moisture Response to Snowmelt and Rainfall in a Sierra Nevada Mixed-Conifer Forest, Vadose Zone J., 10, 10.2136/vzj2011.0001, 786-799.

Banfield, J. F., W. W. Barker, S. A. Welch, and A. Taunton (1999), Biological impact on mineral dissolution: application of the lichen model to understanding mineral weathering in the rhizosphere, Proc Natl Acad Sci USA, 96, 3404–3411.

Bass, J. D. (1995), Elasticity of Minerals, Glasses, and Melts, in Handbook of Physical Constants, edited by T. J. Ahrens, American Geophysical Union, Washington, DC, 45-63.

Bateman, P. C., and D. R. Wones (1972), Geologic map of the Huntington Lake Quadrangle, central Sierra Nevada, California, US Geological Survey.

Befus, K. M., A. F. Sheehan, M. Leopold, S. P. Anderson, and R. S. Anderson (2011), Seismic Constraints on Critical Zone Architecture, Boulder Creek Watershed, Front Range, Colorado, Vadose Zone J., 10, 10.2136/vzj2010.0108, 915-927.

Begonha, A., and S. Braga (2002), Weathering of the Oporto granite: geotechnical and physical properties, Catena, 49, 57-133.

Beylich, A. A., E. Kolstrup, N. Linde, L. B. Pedersen, T. Thyrsted, D. Gintz, and L. Dynesius (2003), Assessment of chemical denudation rates using hydrological measurements, water chemistry analysis and electromagnetic geophysical data, Permafrost and Periglacial Processes, 14, doi:10.1002/ppp.470, 387-397.Burke, B. C., A. M. Heimsath, and A. F. White (2007), Coupling chemical weathering with soil production across soil-mantled landscapes, Earth Surf. Process. Landf., 32, 853-873.

Beylich, A. A., E. Kolstrup, T. Thyrsted, N. Linde, L. B. Pedersen, and L. Dynesius (2004), Chemical denudation in arctic-alpine Latnjavagge (Swedish Lapland) in relation to regolith as assessed by radio magnetotelluric-geophysical profiles, Geomorphology, 57, doi:10.1016/S0169-555X(03)00162-4, 303-319

Brantley, S. L., et al. (2011), Twelve testable hypotheses on the geobiology of weathering, Geobiology, 9, 10.1111/j.1472-4669.2010.00264.x, 140-165.

Braun, J.-J., et al. (2009), Regolith mass balance inferred from combined mineralogical, geochemical and geophysical studies: Mule Hole gneissic watershed, South India, Geochimica et Cosmochimica Acta, 73, 935-961.

Burke, B. C., A. M. Heimsath, and A. F. White (2007), Coupling chemical weathering with soil production across soil-mantled landscapes, *Earth Surf. Process. Landf.*, *32*(6), 853-873.

Buss, H. L., P. B. Sak, S. M. Webb, and S. L. Brantley (2008), Weathering of the Rio Blanco quartz diorite, Luquillo Mountains, Puerto Rico: Coupling oxidation, dissolution, and fracturing, Geochimica et Cosmochimica Acta, 72, 10.1016/j.gca.2008.06.020, 4488-4507.

Buss, H. L., S. L. Brantley, F. N. Scatena, E. A. Bazilievskaya, A. Blum, M. Schulz, R. Jimenez, A. F. White, G. Rother, and D. Cole (2013), Probing the deep critical zone beneath the Luquillo Experimental Forest, Puerto Rico, *Earth Surf. Process. Landf.*, *38*(10), 1170-1186.

Carson, M. A., and M. J. Kirkby (1972), Hillslope Form and Process, 475 pp., Cambridge University Press, London.

Chabaux, F., E. Blaes, P. Stille, R. D. Roupert, E. Pelt, A. Dosseto, L. Ma, H. L. Buss, and S. L. Brantley (2013), Regolith formation rate from U-series nuclides: Implications from the study of a spheroidal weathering profile in the Rio Icacos watershed (Puerto Rico), *Geochimica et Cosmochimica Acta*, *100*, 73-95.

Clarke, B. A., and D. W. Burbank (2011), Quantifying bedrock-fracture patterns within the shallow subsurface: Implications for rock mass strength, bedrock landslides, and erodibility, J. Geophys. Res.-Earth Surf., 116, F04009, 10.1029/2011jf001987.

Dahlgren, R. A., J. L. Boettinger, G. L. Huntington, and R. G. Amundson (1997), Soil development along an elevational transect in the western Sierra Nevada, California, *Geoderma*, *78*(3-4), 207-236.

Davis WM. (1892), The convex profile of bad-land divides, Science, 20, 245–245. DOI: 10.1126/science.ns-20.508.245

Deere, D. U. (1964), Technical description of rock cores, Rock Mech. Engng Geol., 1, 16-22.

Defays, D. (1977), Efficient algorithm for a complete link method, *Computer Journal*, *20*(4), 364-366.

Dethier, D. P., and E. D. Lazarus (2006), Geomorphic inferences from regolith thickness, chemical denudation and CRN erosion rates near the glacial limit, Boulder Creek catchment and vicinity, Colorado, *Geomorphology*, *75*(3-4), 384-399.

Dewandel, B., P. Lachassagne, and R. Wyns (2006), A generalized 3-D geological and hydrogeological conceptual model of granite aquifers controlled by single or multiphase weathering, J. Hydrol., 330, 10.1016/j.jhydrol.2006.03.026, 260-284.

Dietrich, W. E., R. Reiss, M. L. Hsu, and D. R. Montgomery (1995), A process-based model for colluvial soil depth and shallow landsliding using digital elevation data, *Hydrological Processes*, *9*(3-4), 383-400.

Dixon, J. L., A. M. Heimsath, and R. Amundson (2009), The critical role of climate and saprolite weathering in landscape evolution, Earth Surf. Process. Landf., 34, 10.1002/esp.1836, 1507-1521.

Dosseto, A., S. P. Turner, and J. Chappell (2008), The evolution of weathering profiles through time: New insights from uranium-series isotopes, Earth and Planetary Science Letters, 274, 359-371.

Dosseto, A., H. L. Buss, and P. O. Suresh (2012), Rapid regolith formation over volcanic bedrock and implications for landscape evolution, *Earth and Planetary Science Letters*, *337*, 47-55.

Driese, S. G., L. D. McKay, and C. P. Penfield (2001), Lithologic and pedogenic influences on porosity distribution and groundwater flow in fractured sedimentary saprolite: A new application of environmental sedimentology, Journal of sedimentary research, 71, 843-1700.

Ferrier, K. L., J. W. Kirchner, C. S. Riebe, and R. C. Finkel (2010), Mineral-specific chemical weathering rates over millennial timescales: Measurements at Rio Icacos, Puerto Rico, *Chemical Geology*, *277*(1-2), 101-114.

Flint, L. E., and A. L. Flint (2002), Porosity: Calculation from particle and bulk densities, in Methods of Soil Analysis. Part 4: Physical Methods, edited by J. H. Dane and G. C. Topp, pp. 241-242., Soil Science Society of America, Madison, WI.

Gallardo, L. A., and M. A. Meju (2003), Characterization of heterogeneous near-surface materials by joint 2D inversion of dc resistivity and seismic data, Geophysical Research Letters, 30(13).

Gallardo, L. A., and M. A. Meju (2004), Joint two-dimensional DC resistivity and seismic travel time inversion with cross-gradients constraints, J. Geophys. Res.-Solid Earth, 109(B3).

Gassmann, F. (1951), Über die elastizität poröser medien, *Vierteljahrsschrift der Naturforschenden Gesellschaft in Zürich*, *96*, 1-23.

Gilbert, G. K. (1877), Report on the geology of the Henry Mountains, x, 160 p. pp., Govt. print. off., Washington,.

Gilbert, G. K. (1909), The convexity of hilltops, *Journal of Geology*, *17*(4), 344-350.

Gillespie AR, Zehfuss PH. 2004. Glaciations of the Sierra Nevada, California, USA. In Quaternary Glaciations - Extent and Chronology, Part II , Ehlers J and Gibbard PL (eds). Elsevier; 51–62.

Graham, R., A. Rossi, and R. Hubbert (2010), Rock to regolith conversion: Producing hospitable substrates for terrestrial ecosystems, GSA Today, 4-9.

Günther, T., S. Friedel, and K. Spitzer (2003), Estimation of information content and efficiency for different data sets and inversion schemes using the generalized singular value decomposition, presented at the electromagnetic depth sounding workshop, Königstein (Germany).

Günther, T. (2005), Inversion Methods and Resolution Analysis for the 2D/3D Reconstruction of Resistivity Structures from DC Measurements, PhD Thesis, University of Mining and Technology, Freiberg (Germany).

Günther, T., C. Rucker, K. Spitzer (2006), 3-d modeling and inversion of DC resistivity data incorporating topography - Part II: Inversion. Geophys. J. Int.166 , 506-517.

Heimsath, A. M., W. E. Dietrich, K. Nishiizumi, and R. C. Finkel (1997), The soil production function and landscape equilibrium, Nature, 388, 10.1038/41056, 358-361.

Heimsath, A. M., R. A. DiBiase, and K. X. Whipple (2012), Soil production limits and the transition to bedrock-dominated landscapes, *Nature Geoscience*, *5*(3), 210-214.

Heincke, B., T. Guenther, E. Dalsegg, J. S. Ronning, G. V. Ganerod, and H. Elvebakk (2010), Combined three-dimensional electric and seismic tomography study on the Aknes rockslide in western Norway, J. Appl. Geophys., 70(4), 292-306.

Helgerud, M. B. (2001), Wave speeds in gas hydrates and sediments containing gas hydrate: A laboratory and modeling study, Ph.D. thesis, 249 pp, Stanford University, Stanford, CA, available at http://stanford.io/15uCj6B.

Helgerud, M. B., J. Dvorkin, A. Nur, A. Sakai, and T. Collett (1999), Elastic-wave velocity in marine sediments with gas hydrates: Effective medium modeling, Geophysical Research Letters, 26, 2021–2024.

Hill, R. (1952), The elastic behavior of crystalline aggregate, Proc. Phys. Soc. London, A65, 349–354.

Hubbert, K., R. Graham, and M. Anderson (2001), Soil and weathered bedrock: Components of a Jeffrey pine plantation substrate, Soil Science Society of America Journal, 65, 4.

Hunsaker, C. T., and S. M. Eagan (2003), Small stream ecosystem variability in the Sierra Nevada of California, in First Interagency Conference on Research in the Watersheds, edited by K. G. Renard, pp. 716-721, USDA-ARS, , Washington, DC.

Hunsaker, C. T., T. W. Whitaker, and R. C. Bales (2012), Snowmelt Runoff and Water Yield Along Elevation and Temperature Gradients in California's Southern Sierra Nevada, Journal of the American Water Resources Association10.1111/j.1752-1688.2012.00641.x., 1-12.

Jessup, B. S., W. J. Hahm, S. N. Miller, J. W. Kirchner, and C. S. Riebe (2011), Landscape response to tipping points in granite weathering: The case of stepped topography in the Southern Sierra Critical Zone Observatory, Applied Geochemistry, 26, 10.1016/j.apgeochem.2011.03.026, S48-S50.

Johnson, D. W., C. T. Hunsaker, D. W. Glass, B. M. Rau, and B. A. Roath (2011), Carbon and nutrient contents in soils from the Kings River Experimental Watersheds, Sierra Nevada Mountains, California, Geoderma, 160, 10.1016/j.geoderma.2010.10.019, 490-502.

Johnson, T. C., L. D. Slater, D. Ntarlagiannis, F. D. Day-Lewis, and M. Elwaseif (2012), Monitoring groundwater-surface water interaction using time-series and time-frequency analysis of transient three-dimensional electrical resistivity changes, Water Resour. Res., doi:10.1029/2012WR011893, in press.

Knight, R., et al. (2010), Geophysics at the interface: Response of geophysical properties to solid-fluid, fluid-fluid, and solid-solid interfaces, *Reviews of Geophysics*, *48*.

LaBrecque, D., and S. Ward (1990), 2-D cross-borehole resistivity model fitting: In Ward, S (Ed.), Geotechnical and Environmental Geophysics, SEG, Tulsa, OK, 51-47.Landeweert, R., E. Hoffland, R. D. Finlay, T. W. Kuyper, and N. van Breemen (2001), Linking plants to rocks: ectomycorrhizal fungi mobilize nutrients from minerals, Trends Ecol. Evol., 16, 10.1016/s0169-5347(01)02122-x, 248-254.

Landeweert, R., E. Hoffland, R. D. Finlay, T. W. Kuyper, and N. van Breemen (2001), Linking plants to rocks: ectomycorrhizal fungi mobilize nutrients from minerals, *Trends Ecol. Evol.*, *16*(5), 248-254.

Lebedeva, M., R. Fletcher, and S. Brantley (2010), A mathematical model for steady state regolith production at constant erosion rate, Earth Surf. Process. Landf., 35, 10.1002/esp.1954, 508-1032.

Lin, H., J. W. Hopmans, and D. d. Richter (2011), Interdisciplinary Sciences in a Global Network of Critical Zone Observatories, Vadose Zone J., 10, 10.2136/vzj2011.0084, 781-785.

Loke, M. H. (2004), 2-D and 3-D electrical imaging surveys, (PDF available from http://www.geoelectrical.com/).

Loke, M. H., I. Acworth, and T. Dahlin (2003), A comparison of smooth and blocky inversion methods in 2-D electrical imaging surveys, Exploration Geophysics, 34, 182–187.

Ma, L., F. Chabaux, E. Pelt, E. Blaes, L. X. Jin, and S. Brantley (2010), Regolith production rates calculated with uranium-series isotopes at Susquehanna/Shale Hills Critical Zone Observatory, *Earth and Planetary Science Letters*, *297*(1-2), 211-225.

Marechal, J. C., B. Dewandel, K. Subrahmanyam, and R. Torri (2003), Specific methods for the evaluation of hydraulic properties in fractured hard-rock aquifers, Current Science, 85, 511-516.

Marechal, J. C., B. Dewandel, and K. Subrahmanyam (2004), Use of hydraulic tests at different scales to characterize fracture network properties in the weathered-fractured layer of a hard rock aquifer, Water Resour. Res., 40, W11508, 10.1029/2004wr003137.

Mavko, G., and T. Mukerji (1998), Bounds on low-frequency seismic velocities in partially saturated rocks, Geophysics, 63, 918.

McClymont, A. F., J. W. Roy, M. Hayashi, L. R. Bentley, H. Maurer, and G. Langston (2011), Investigating groundwater flow paths within proglacial moraine using multiple geophysical methods, J. Hydrol., 399(1-2), 57-69.

Mindlin, R. D. (1949), Compliance of elastic bodies in contact, J. Appl. Mech.-Trans. ASME, 16, 259-268.

Molnar, P., R. S. Anderson, and S. P. Anderson (2007), Tectonics, fracturing of rock, and erosion, J. Geophys. Res.-Earth Surf., 112, F03014, 10.1029/2005jf000433.

Moser, T. J. (1991), Shortest path calculation of seismic rays, Geophysics, 56, 59–67.

National Research Council (2001), Basic research opportunities in earth science, National Acadamy Press, Washington, DC.

Nur, A., G. Mavko, J. Dvorkin, and D. Galmudi (1998), Critical Porosity: A Key to Relating Physical Properties to Porosity in Rocks, The Leading Edge, 17, 357-362.

Oldenburg, D. W., and Y. G. Li (1999), Estimating depth of investigation in dc resistivity and IP surveys, Geophysics, 64, 10.1190/1.1444545, 403-416.

Olhoeft, G. R. (1981), Electrical properties of granite with implications for the lower crust, Journal of Geophysical Research, 86, 10.1029/JB086iB02p00931, 931-936.

Olona, J., J. A. Pulgar, G. Fernandez-Viejo, C. Lopez-Fernandez, and J. M. Gonzalez-Cortina (2010), Weathering variations in a granitic massif and related geotechnical properties through seismic and electrical resistivity methods, Near Surf. Geophys., 8, 10.3997/1873-0604.2010043, 585-599.

Oster, J. L., I. P. Montanez, W. D. Sharp, and K. M. Cooper (2009), Late Pleistocene California droughts during deglaciation and Arctic warming, *Earth and Planetary Science Letters*, *288*(3-4), 434-443.

Rasmussen, C., S. Brantley, D. D. Richter, A. Blum, J. Dixon, and A. F. White (2011), Strong climate and tectonic control on plagioclase weathering in granitic terrain, *Earth and Planetary Science Letters*, *301*(3-4), 521-530.

Rawlinson, N., S. Pozgay, and S. Fishwick (2010), Seismic tomography: A window into deep Earth, Physics of the Earth and Planetary Interiors, 178, 10.1016/j.pepi.2009.10.002, 101-135.

Riebe, C. S., J. W. Kirchner, D. E. Granger, and R. C. Finkel (2000), Erosional equilibrium and disequilibrium in the Sierra Nevada, inferred from cosmogenic Al-26 and Be-10 in alluvial sediment, *Geology*, *28*(9), 803-806.

Riebe, C. S., J. W. Kirchner, D. E. Granger, and R. C. Finkel (2001), Strong tectonic and weak climatic control of long-term chemical weathering rates, *Geology*, *29*(6), 511-514.

Riebe, C. S., J. W. Kirchner, and R. C. Finkel (2003), Long-term rates of chemical weathering and physical erosion from cosmogenic nuclides and geochemical mass balance, *Geochimica et Cosmochimica Acta*, *67*(22), 4411-4427.

Riebe, C. S., J. W. Kirchner, and R. C. Finkel (2004), Erosional and climatic effects on long-term chemical weathering rates in granitic landscapes spanning diverse climate regimes, *Earth and Planetary Science Letters*, *224*(3-4), 547-562.

Riebe, C. S., and D. E. Granger (2013), Quantifying effects of deep and near-surface chemical erosion on cosmogenic nuclides in soils, saprolite, and sediment, *Earth Surf. Process. Landf.*, *38*(5), 523-533.

Robinson, D. A., et al. (2008), Advancing process-based watershed hydrological research using near-surface geophysics: a vision for, and review of, electrical and magnetic geophysical methods, Hydrological Processes, 22, 10.1002/hyp.6963, 3604-3635.

Ruxton, B. P., and L. Berry (1957), Weathering of granite and associated erosional features in Hong Kong, *Geological Society of America Bulletin*, *68*(10), 1263-&.

Saarenketo, T. (1998), Electrical properties of water in clay and silty soils, J. Appl. Geophys., 40, 73-88.

Samouëlian, A., I. Cousin, A. Tabbagh, A. Bruand, and G. Richard (2005), Electrical resistivity survey in soil science: a review, Soil and Tillage research, 83, 10.1016/j.still.2004.10.004, 173-366.

Slater, L., and A. Binley (2006), Engineered barriers for pollutant containment and remediation in: Vereeken, H., Binley, A., Cassiani, G., Revil, A. Titov, K. (Eds.), Applied Hydrogeophysics, NATO Science Series IV, Earth and Environmental Sciences, Springer, 293-317.

Stallard, R. F. (1985), River Chemistry, Geology, Geomorphology, and Soils in the Amazon and Orinoco Basins, in The Chemistry of Weathering, edited by J. I. Drever, pp. 293-316, D. Reidel Publishing Company.

Stallard, R. F., and J. M. Edmond (1983), Geochemistry of the Amazon 2: The influence of geology and weathering environment on the dissolved-load, Journal of Geophysical Research-Oceans and Atmospheres, 88, 9671-9688.

Stock, G. M., R. S. Anderson, and R. C. Finkel (2004), Pace of landscape evolution in the Sierra Nevada, California, revealed by cosmogenic dating of cave sediments, *Geology*, *32*(3), 193-196.

Stonestrom, D. A., A. F. White, and K. C. Akstin (1998), Determining rates of chemical weathering in soils - solute transport versus profile evolution, J. Hydrol., 209, 331-345.

Taylor, R., and K. Howard (2000), A tectono-geomorphic model of the hydrogeology of deeply weathered crystalline rock: evidence from Uganda, Hydrogeol. J., 8, 279-573.

Wahrhaftig, C. (1965), Stepped topography of southern Sierra Nevada California, Geological Society of America Bulletin, 76, 10.1130/0016-7606, 1165 - 1190.

White, A. F., A. E. Blum, M. S. Schulz, D. V. Vivit, D. A. Stonestrom, M. Larsen, S. F. Murphy, and D. Eberl (1998), Chemical weathering in a tropical watershed, Luquillo mountains, Puerto Rico: I. Long-term versus short-term weathering fluxes, *Geochimica et Cosmochimica Acta*, *62*(2), 209-226.

Winter, T. C. (1999), Relation of streams, lakes, and wetlands to groundwater flow systems, Hydrogeol. J., 7, 10.1007/s100400050178, 28-45.

Yoo, K., S. M. Mudd, J. Sanderman, R. Amundson, and A. Blum (2009), Spatial patterns and controls of soil chemical weathering rates along a transient hillslope, Earth and Planetary Science Letters, 288, 184-377.

Soil Depth (m)	Type	g cm^{-3}		cm^3 cm^{-3}		cm^3 cm^{-3}		%
		Mean ρ_b	σ	Mean φ	σ	Mean VWC	σ	Saturation
0.3	Auger	1.27	0.14	0.52	0.05	0.13	0.05	0.25
0.6	Auger	1.43	0.18	0.46	0.07	0.11	0.01	0.24
0.75	Auger	1.30		0.51		0.11		0.22
0.9	Auger	1.39	0.15	0.48	0.06	0.12	0.02	0.25
1.2	Auger	1.51	0.07	0.43	0.03	0.15	0.03	0.34
1.5	Auger	1.52	0.13	0.43	0.05	0.16	0.04	0.38
1.8	Auger	1.44	0.10	0.46	0.04	0.18	0.01	0.40
2	Auger	1.44	0.17	0.46	0.07	0.14	0.05	0.31
0.7	Geoprobe	0.96		0.64		0.07		0.12
1.7	Geoprobe	1.28		0.52		0.12		0.23
2.7	Geoprobe	1.27		0.52		0.13		0.25
3.7	Geoprobe	1.12		0.58		0.16		0.28
4.7	Geoprobe	1.35		0.49		0.18		0.38
5.7	Geoprobe	1.36		0.49		0.17		0.35
6.7	Geoprobe	1.38		0.48		0.19		0.40
7.7	Geoprobe	1.49		0.44		0.21		0.48
8.7	Geoprobe	1.58		0.40		0.27		0.67
9.7	Geoprobe	1.72		0.35		0.35		0.99
10.2	Geoprobe	1.64		0.38		0.33		0.87

Table 1. Mean bulk density and porosity values with standard deviations (σ, calculated where possible) for hand-auger and Geoprobe samples used in this paper. VWC = Volumetric Water Content = water filled porosity; Saturation = percent of pore space occupied by water
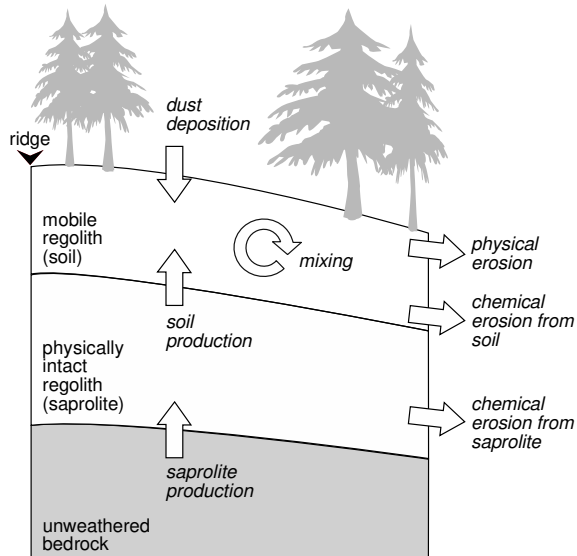
Figure 1. Concept sketch showing material components and fluxes of the "critical zone" (CZ), which here refers inclusively to regolith and overlying vegetation, following widespread use of the term in the literature (National Research Council, 2001; Brantley et al., 2011). Regolith is the heterogeneous interface between air and rock – a blanket of weathered material that includes saprolite and soil. Its thickness changes when there is an imbalance between inputs and outputs (denoted by arrows). Soil refers to the uppermost, mobile layer of weathered rock, organic detritus, and allochthonous dust, without regard to its degree of chemical alteration and horizonation. It is generated from above, by dust deposition, and from below, by breakdown of saprolite. Transport downslope results in mixing; losses occur by chemical and physical erosion. Saprolite differs from overlying soil in that it is static enough to retain the fabric of underlying bedrock. The production or saprolite at the rock-regolith interface is counteracted by losses due to production of soil and chemical erosion.
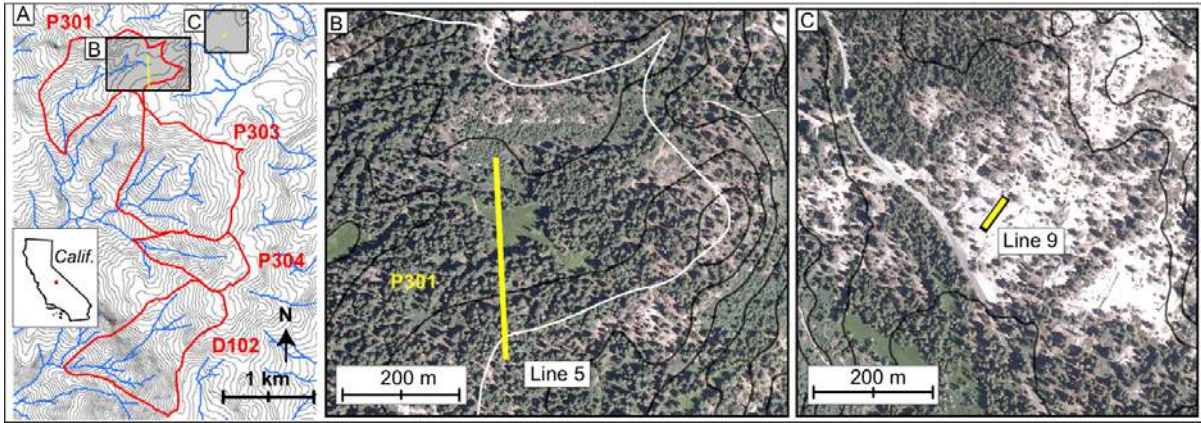
Figure 2. Location map, showing CZO catchments (A), which drain to Providence and Duff creeks in granitic terrain of the Southern Sierra Nevada. Line 5 is located at the head of catchment P301 (with drainage divide shown in white), spanning a heavily instrumented swampy meadow and forested slope (B). Line 9 (C) spans an expanse of bare bedrock near Glen Meadow. Contour interval (black lines) is 10 m in each panel.
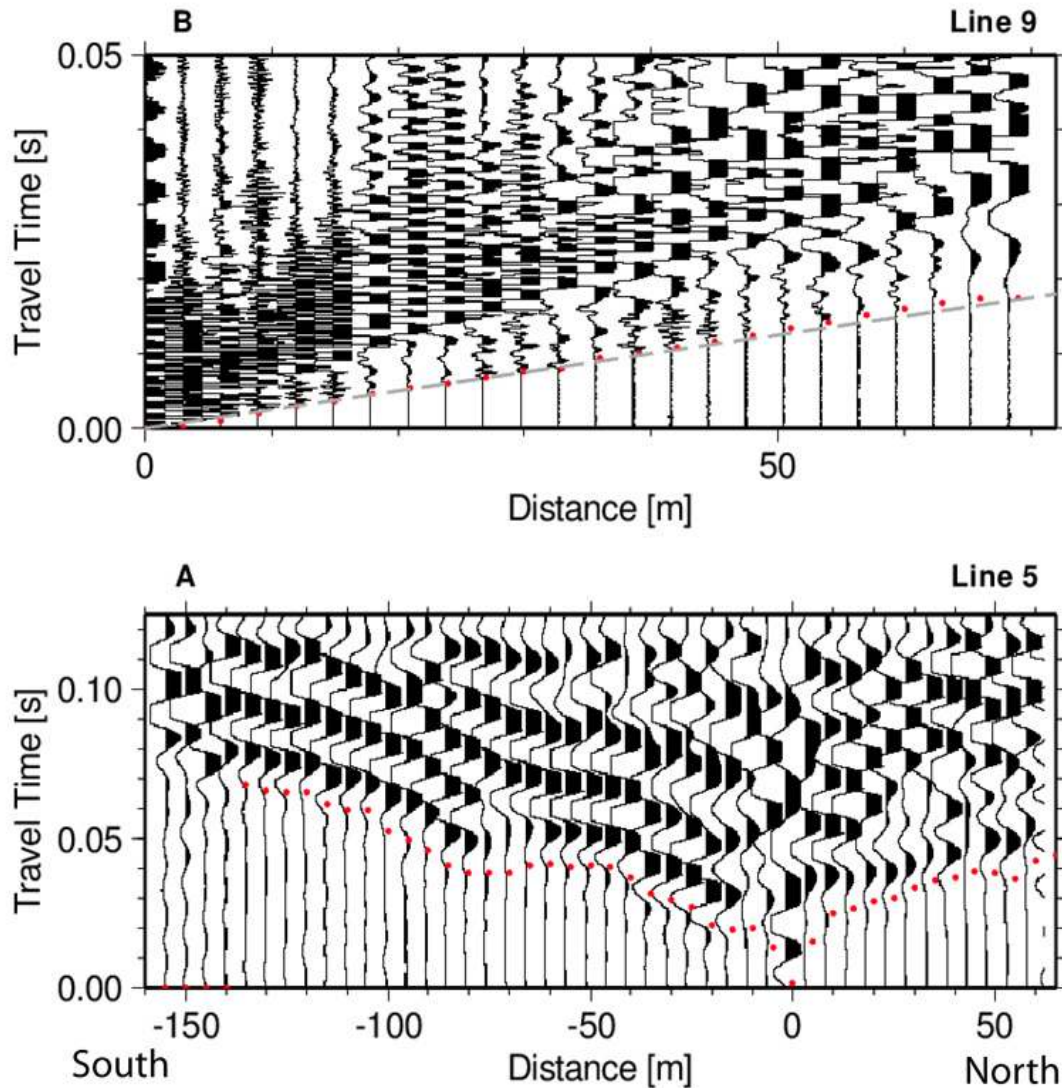
Figure 3. Seismic refraction data from geophones for one set of stacked records from (A) Line 5, and (B) Line 9. X axis is distance away from source at X = 0. Data quality is typical of stacked shots at other locations and is generally sufficient for straightforward manual picking of first arrivals (here marked by dots on each plot). Dashed line on data from Line 9, which spans a bare bedrock ridge, has a slope of 4 km/s and is consistent with manually picked first arrivals. The same strong match to a 4 km/s slope can be seen on all of the stacked records for Line 9, implying that 4 km/s at depth is representative of minimally altered and fractured granite at the site. Note scale change between the data plots.
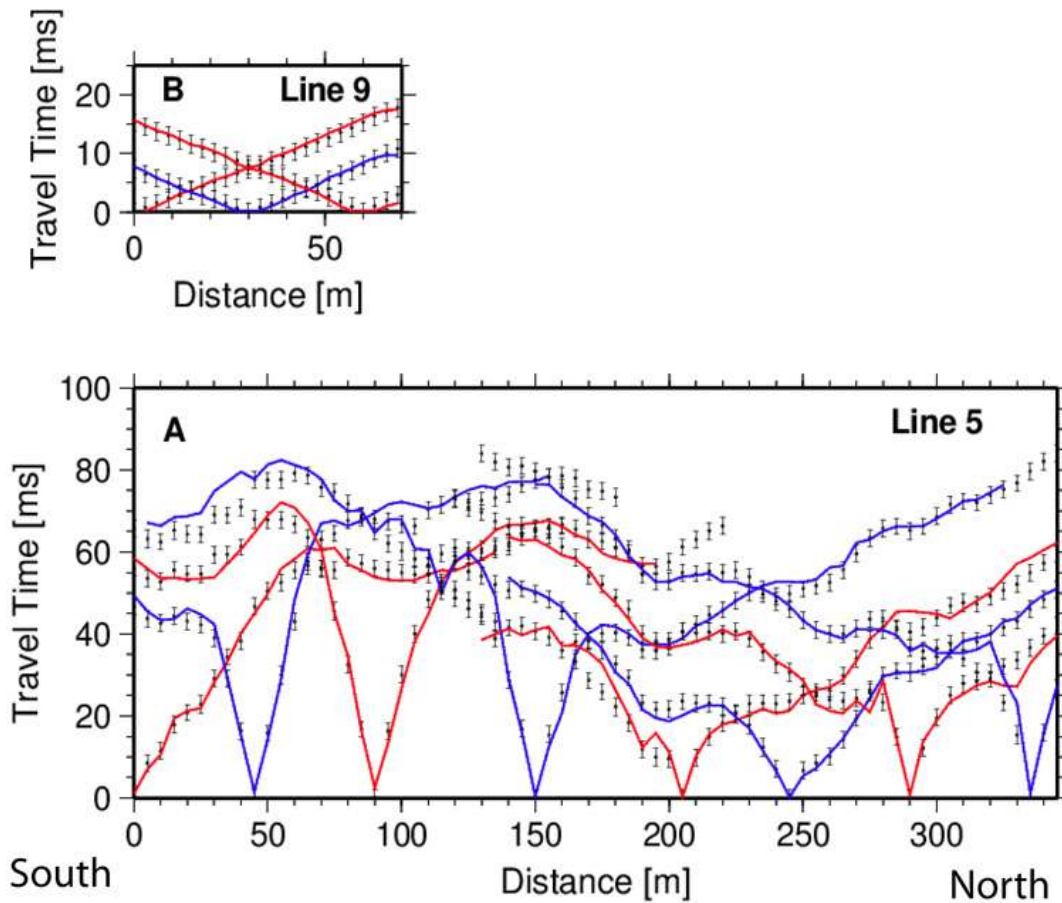
Figure 4. Travel time plots for (A) Line 5 and (B) Line 9, showing observed first-arrival travel times (dots with error bars) and predicted travel times based on the best-fit velocity models (red or blue lines). The observed and predicted travel times match well, suggesting that the inverted velocity model (Figure 5) is acceptable. To maintain clarity, only a subset (about 20%) of the shots are plotted here. Note scale change between plots.
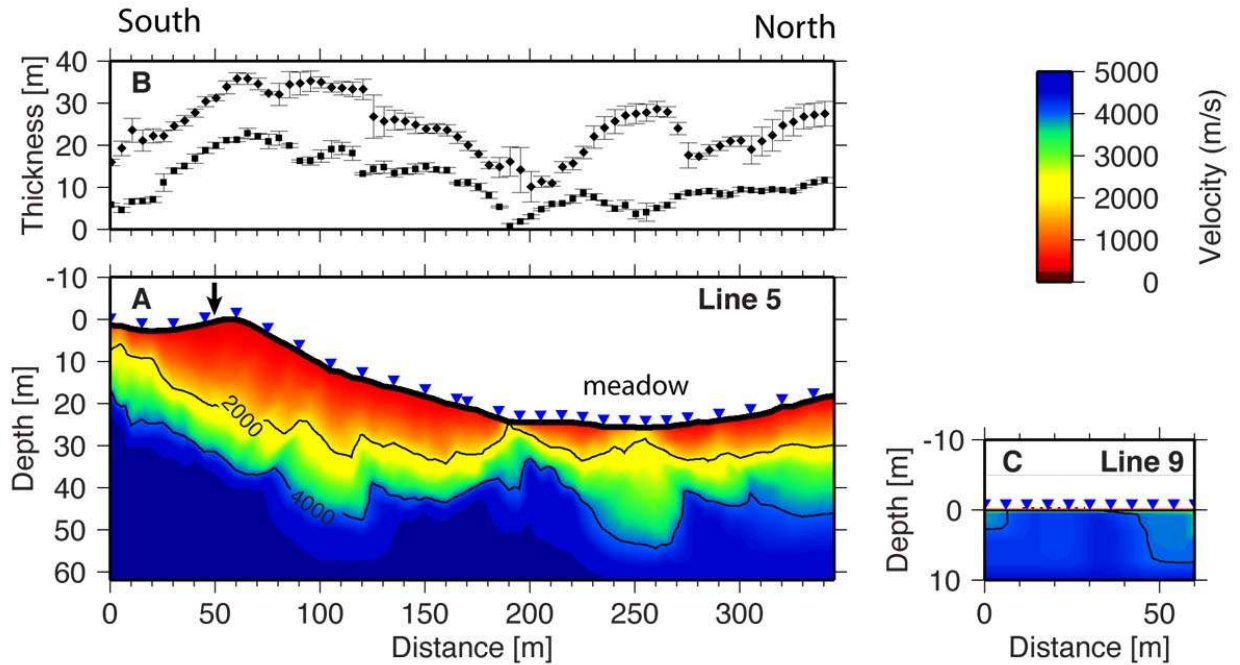
Figure 5. (A) Velocity model of Line 5 from inversion of first-arrival travel times. (B) Depth from the surface to the 2000 m/s and 4000 m/s contours. Error bars reflect variations observed in an ensemble of solutions that result from a range of starting models (see text). Depth to the 4000 m/s contour varies from 10 to 35 m (average 23 m) and is highest at the crest of the forested slope, under CZT-1 (denoted by arrow), a heavily instrumented white fir. In contrast, under the swampy meadow, depth to the 4000 m/s contour is shallowest and most variable, ranging from ~10 to 30 m over just 60 m of horizontal distance. (C) Velocity model of Line 9 from inversion of first-arrival travel times. Velocities of 4000 m/s at the surface on Line 9, acquired on an extensive granite outcrop (Fig. 2C), enable interpretation of 4000 m/s velocities (blue shades) on Line 5 as coherent bedrock at depth.
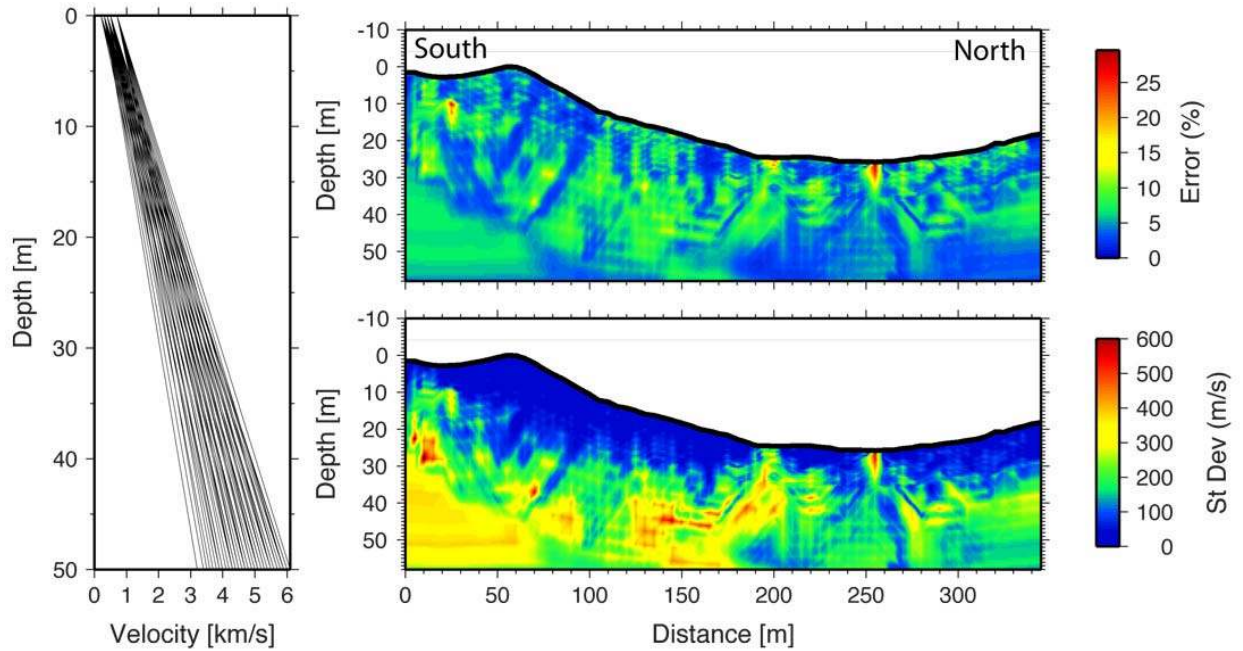
Figure 6. Results of sensitivity analysis of uncertainties in seismic velocity on Line 5. (Left) Velocity-depth gradients (in depth below surface) of 50 starting models used to generate ensemble of inverted models. (Right) Variance among final inversion in ensemble, expressed as standard deviation (bottom) and percent error (top). Velocity sensitivity in the upper 10 m is generally ±100 m/s or less, and ±300 m/s or more elsewhere.
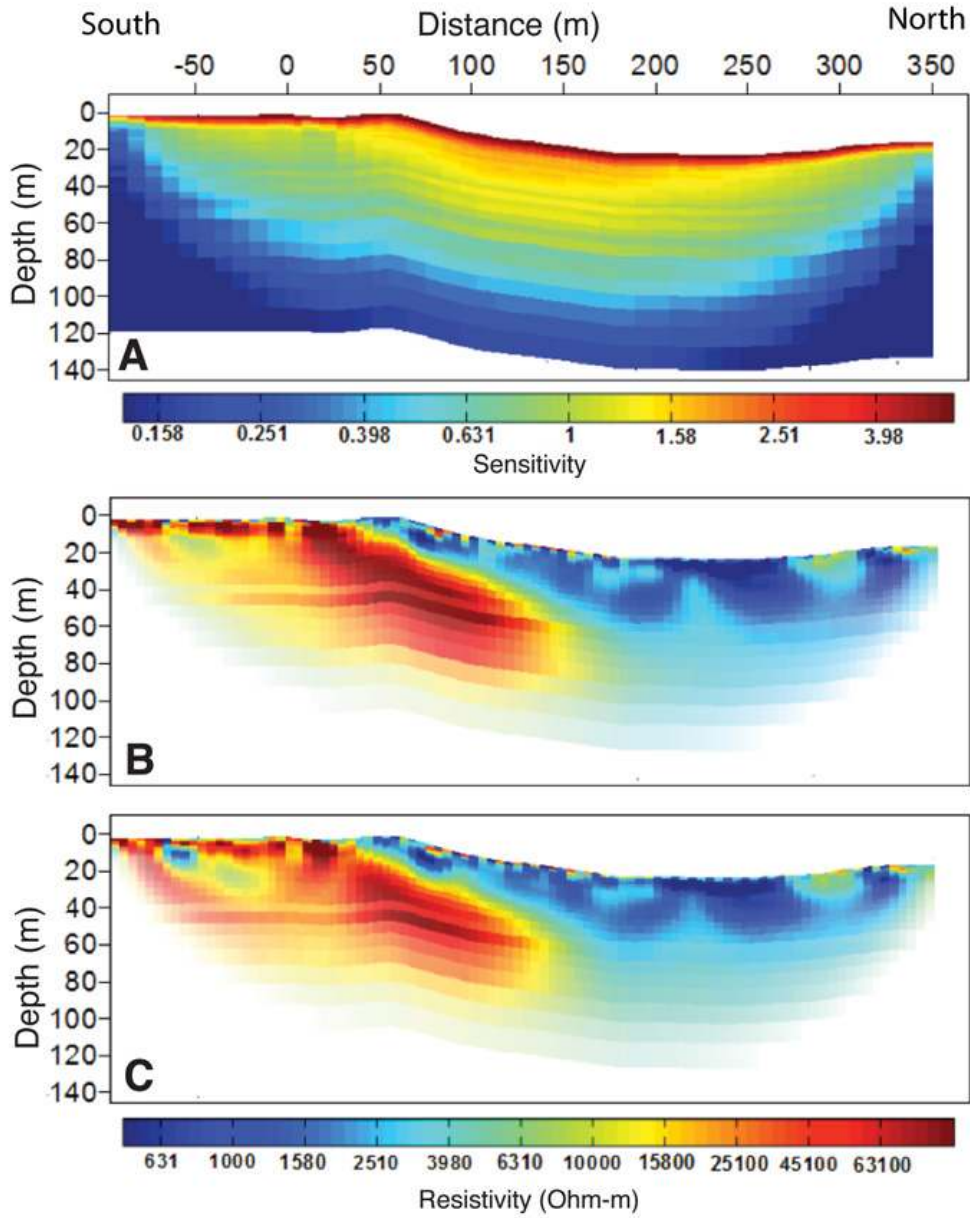
Figure 7. Results of the sensitivity analysis. (A) Sensitivity model, (B) smooth inversion model assuming 2000 ohm-m homogenous initial model and (C) smooth inversion model assuming 5000 ohm-m homogenous initial model.
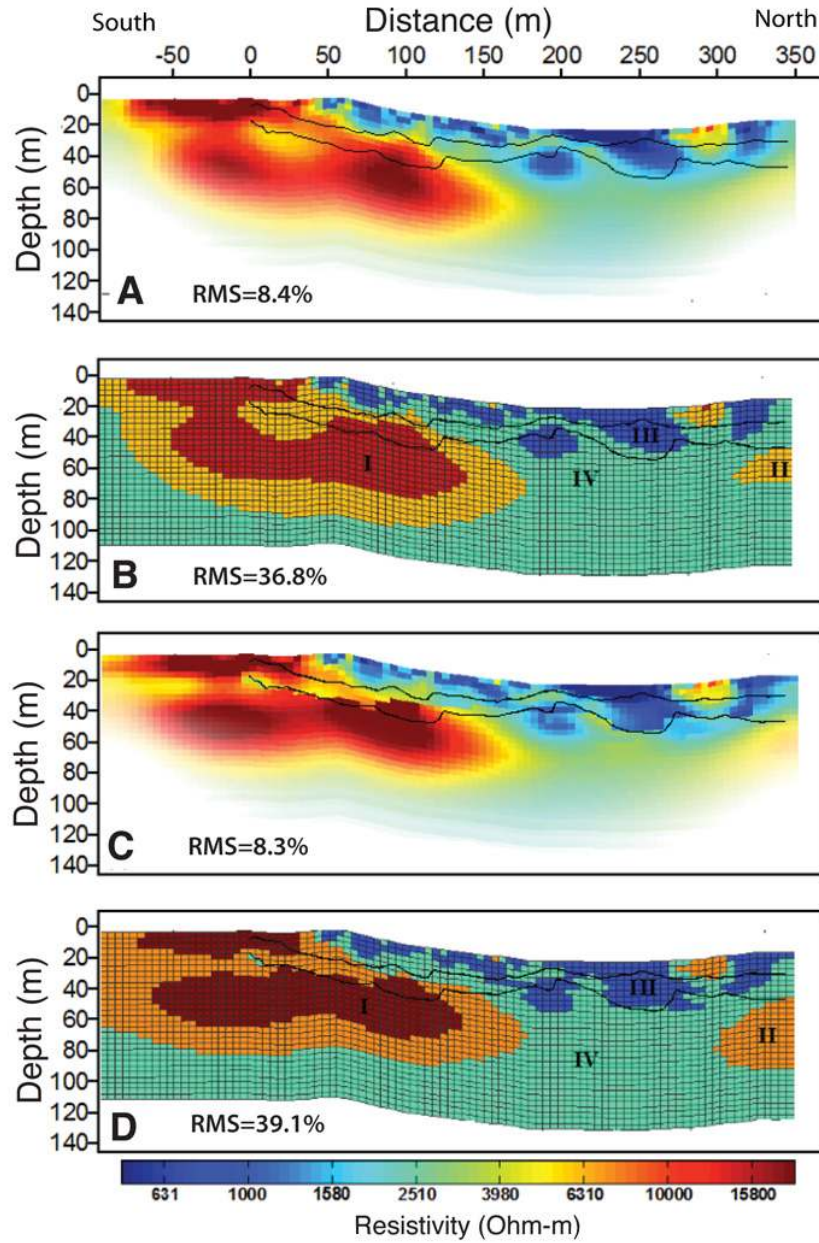
Figure 8. Inversion results of Line 5 data (A) smooth inversion, (B) cluster analysis based on the resistivity model in 'a', (C) disconnect inversion, and (D) cluster analysis based on the resistivity model in 'c'. Lines show locations of the 2 km/s and 4 km/s velocity contours within the resistivity model space. Note that all images have the same color scale.
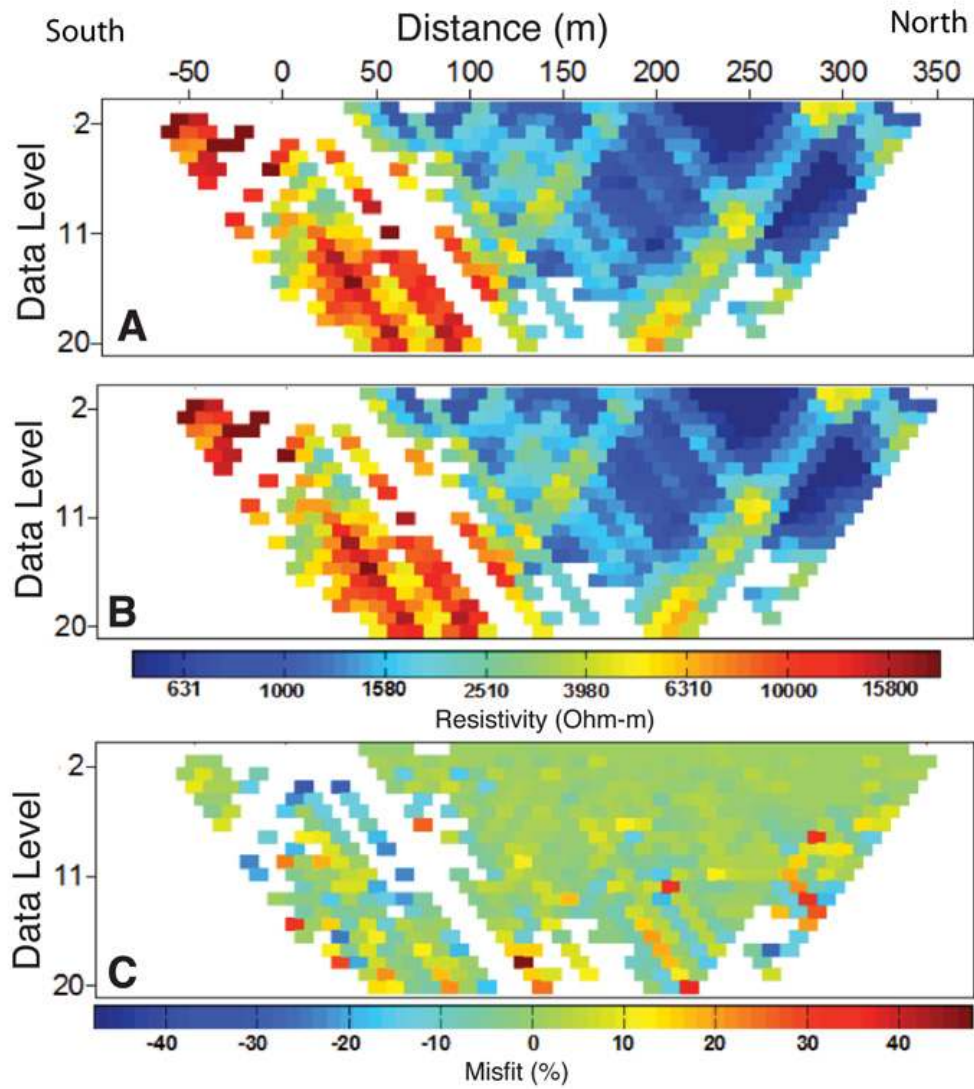
Figure 9. Data misfit for the smoothness constraint inversion model. (A) Observed data, (B) predicted data and (C) misfit between the observed and predicted data. The predicted data is consistent with the observed data except at areas of low data coverage.
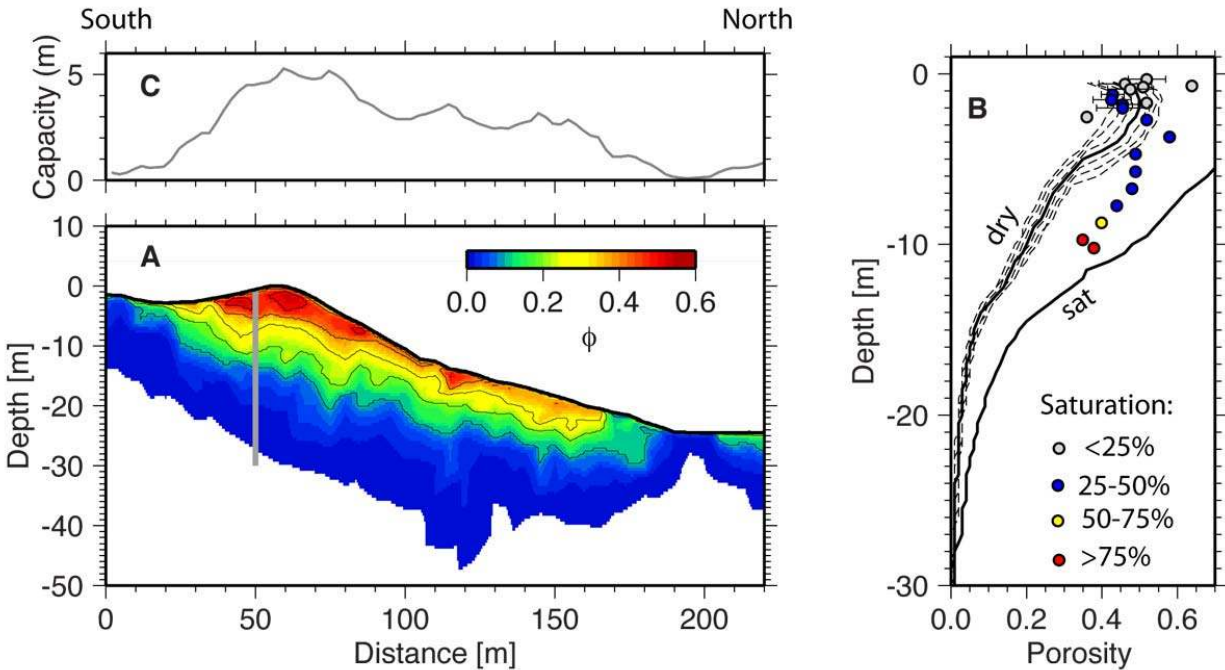
Figure 10. Interpretation of geophysical data and analysis of bulk samples from Line 5. (A) Porosity model on southern portion of Line 5, calculated from seismic velocities using a rock physics model, and assuming dry porosity and a composition of 50% feldspar, 25% quartz, and 25% clay. Porosity is contoured every 0.1 (10%). These are minimum values for porosity for this composition; if pore space is saturated, higher porosities would be needed to match seismic velocities. White region at base shows area where porosity is predicted to be zero (that is, at the bedrock-regolith interface). (B) Predicted porosity-depth profiles at the location of the gray line in figure A, near the white fir CZT-1, for dry porosity ("dry") and water-saturated porosity ("sat"). Solid lines show the predicted porosity for the composition assumed in part A; dashed lines show sensitivity of porosity calculation to variation in composition over a range of 25-50% quartz, 10-65% feldspar, and 0-65% clay (shown only for dry porosity model). Circles mark porosities (± standard deviations where available) measured from volumetric samples of saprolite (see text), color-coded by measured saturation values (Table 1) as indicated in legend. The minimum-porosity model provides good agreement with measured porosities in the upper 3 m, where porosity is mostly dry. At deeper depths, porosities are closer to the saturated model, as expected given the increase in measured saturation of samples with depth. (C) Total water storage capacity of the subsurface, in meters of water, calculated by integrating porosity profiles

with depth at all positions across the model. At the top of the hill near CZT-1, the subsurface could hold a minimum of ~5 m^3/m^2 of water if fully saturated; over the entire profile, the minimum water holding capacity is averages ~3 m^3/m^2.
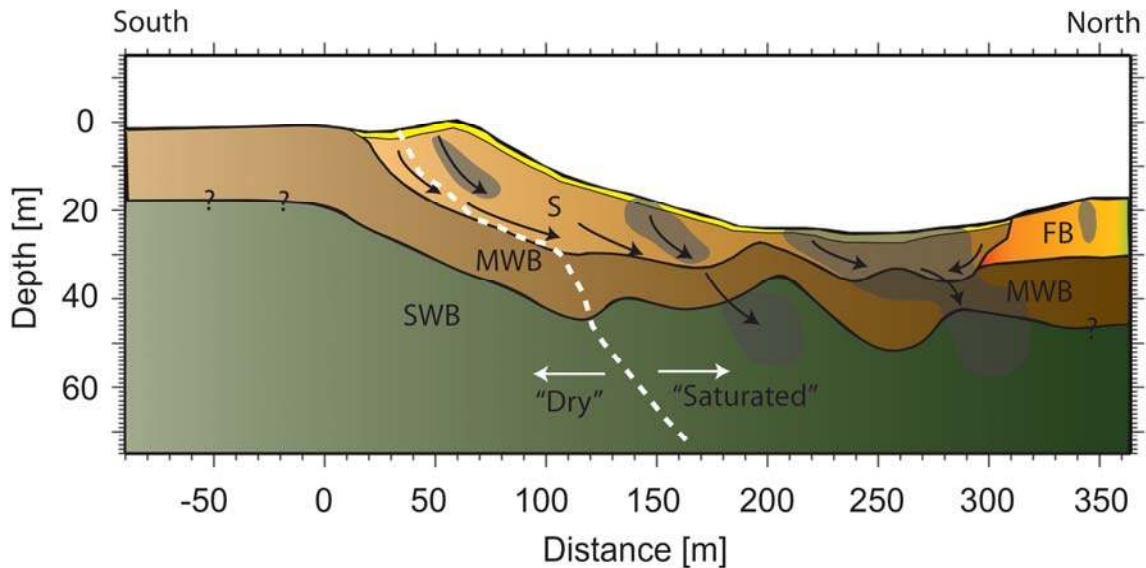

Figure 11. Interpretive cross section of Line 5, based on seismic velocity and resistivity data. Vertical stratification based primarily on seismic velocities (Vp) and are approximate depths of more gradational transitions between saprolite (S, Vp < 2 km/s), moderately weathered bedrock (MWB, 2 km/s < Vp < 4 km/s), and more-or-less unweathered bedrock (UB, Vp > 4 km/s). White dashed line shows approximate boundary at the time of our survey between dominantly unsaturated pore space ("dry") and largely saturated pore space, as indicated by the lateral transition from high to low resistivity (Fig. 8). FB is a fractured bedrock unit exposed on the surface, which has low Vp but high resistivity. Gray zones are locations of highly conductive (<500 ohm-m) bodies resolved in the resistivity model. Black arrows show speculative sense of subsurface water flow. The symbols '?' denote locations where interpretation is based on resistivity data alone.